

On the properties of discs around accreting brown dwarfs

Nathan J. Mayne^{*} and Tim J. Harries

School of Physics, University of Exeter, Stocker Road, Exeter, EX4 4QL.

Accepted ?. Received ?; in original form ?

ABSTRACT

We present a grid of models of accreting brown dwarf systems with circumstellar discs. The calculations involve a self-consistent solution of both vertical hydrostatic and radiative equilibrium along with a sophisticated treatment of dust sublimation. We have simulated observations of the spectral energy distributions and several broad-band photometric systems. Analysis of the disc structures and simulated observations reveal a natural dichotomy in accretion rates, with $\log \dot{M} > -9$ and ≤ -9 classed as extreme and typical accretors respectively. Derivation of ages and masses from our simulated photometry using isochrones is demonstrated to be unreliable even for typical accretors. Although current brown dwarf disc candidate selection criteria have been shown to be largely reliable when applied to our model grid we suggest improved selection criteria in several colour indices. We show that as accretion rates increase brown dwarf disc systems are less likely to be correctly identified. This suggests that, within our grid, systems with higher accretion rates would be preferentially lost during brown dwarf target selection. We suggest that observations used to assert a $\dot{M} \propto M_*^2$ relationship may contain an intrinsic selection bias.

Key words: stars:evolution – stars:formation – stars: pre-main-sequence – techniques: photometric – catalogues – (stars) Hertzsprung-Russell H-R diagram

1 INTRODUCTION

There is now strong evidence that as brown dwarfs (BDs) form they pass through a classical T Tauri star (CTTS) phase, during which they possess a flared, dusty circumstellar disc from which they are actively accreting material (Jayawardhana et al. 2003; Mohanty et al. 2004). The accretion is thought to proceed via a magnetically-controlled funnel flow mechanism in which material from a truncated inner disc boundary falls onto the surface of the star along magnetic field lines (Camenzind 1990; Koenigl 1991; Muzeirole et al. 2003; Mohanty & Shu 2008).

The interpretation of the spectral energy distributions (SEDs) of pre-main-sequence (pre-MS) stars involves trying to distinguish the various contributions to the continuum from the hot spots at the base of the accretion flow, the photospheric flux, and the near-IR flux from the dusty inner disc. The complexity of the interplay between these contributions is exacerbated by other geometrical effects such as the inclination (which changes the projected area of the inner disc wall visible to the observer) and the outer disc

structure (which may obscure the inner disc for high inclinations Walker et al. 2004; Tannirkulam et al. 2007).

In surveys, particularly those attempting to discern the pre-MS disc fraction disentangling of the SED components usually takes place using broad-band photometric measures and cuts in colour-colour or colour-magnitude space (Luhman et al. 2005, 2008; Gutermuth et al. 2008; Monin et al. 2010). The important quantity here is the separation in wavelength between the emission peaks for the stellar and thermal disc components, as it is these components which must be isolated. For BD disc (BDD hereafter) systems it is likely that difficulties detecting the disc will be exacerbated by the lower temperatures of the photosphere and therefore the smaller separation in wavelength from the thermal disc emission component, compared to CTTS systems. Therefore, to derive disc fractions for BD populations we require detailed comparison models with which to guide disc candidate selection.

Comparison of accretion rates across the pre-MS mass spectrum has indicated that the accretion rate is strongly correlated with pre-MS mass, (Muzeirole et al. 2003; Natta et al. 2004, 2006), with an approximate form $\dot{M}_{\text{acc}} \propto M_*^2$. Since in the canonical picture the accretion rate is driven by the disc viscosity, and should be independent of the mass of

^{*} E-mail: nathan@astro.ex.ac.uk (NJM)

the central object, this correlation is somewhat surprising. There is some danger that the correlation is the result of, or at least strengthened by, the presence of observational biases (Clarke & Pringle 2006). At the high-mass (CTTS) end of the mass spectrum the lowest accretion-rates cannot be measured via continuum methods since the excess is too small in contrast with the photospheric emission. The emission lines will also be weak, and indeed the H α equivalent width (EW) may be less than the 10Å that traditionally demarcates classical from weak-lined T Tauri stars (although this boundary may well be spectral type dependent, Barrado y Navascués & Martín 2003). Such objects should show doppler-broadened profiles, but the line wings will be weak, and the presence of underlying H α absorption may become dominant. Thus there may well be a population of low-accretion-rate CTTS which are current missing from the surveys.

There are also risks of observational biases at the low-mass end of the correlation. Radiative-transfer modelling of H α emission from accreting BDs requires high temperatures (> 10 kK) in the accretion funnels in order to recover the level of emission that is observed (Muzerolle et al. 2003; Natta et al. 2004, 2006). Although cooling rate arguments can be invoked to explain the presence of such high temperatures, the line ratios of Pa β and Br γ indicate that the hydrogen emission may not arise in the funnel flows (Gatti et al. 2006). However, recently some continuum measurements of accreting BDs have been conducted (Herczeg et al. 2009), and these broadly support the H α rates.

Nonetheless it is worth considering the observed effect that mass accretion at typical CTTS rates onto a BD might have. Parity between the BD photospheric luminosity and the accretion luminosity occurs at relatively low accretion rates (Clarke & Pringle 2006) and such objects may not be detected as BDs at all in photometric surveys. Even before such an extreme case is reached, the additional luminosity provided by the accretion should have measurable effect on the BD colours. Furthermore the additional flux will be reprocessed by the disc, altering its scaleheight and possibly the shape of its inner edge.

Here we present a grid of models of BDD systems, including a self-consistent treatment of the photospheric and accretion luminosity sources and the interaction of that flux with the circumstellar disc. We investigate the impact of the luminosity of the central source on location and shape of the disc inner rim, as well as the large-scale structure and flaring of the outer disc. We construct synthetic colour-colour and colour-magnitude diagrams in order to examine the efficacy of the photometric selections used to isolate brown dwarfs and measure disc fractions (Luhman et al. 2005, 2008; Gutermuth et al. 2008; Monin et al. 2010).

The complete model grid, with derived photometry and isochrones, is available online through our browsing tool¹ which is described in Appendix A.

2 MODEL

In this section we detail the physical model adopted and assumptions made (Section 2.1), then explain key elements of the radiative transfer code (Section 2.2). Then we discuss the derived values, such as broadband photometric magnitudes and colours (in Section 2.3). Some internal consistency checks are given in Appendix B.

2.1 Physical model and assumptions

2.1.1 Photospheric flux

In order to model an accreting BDD system one must first model the underlying photospheric flux. We have adopted a BD stellar interior and atmospheric model grid and have then constructed the total photospheric flux for any input value of stellar age and mass by interpolating for surface gravity ($\log g$), effective temperature (T_{eff}), radius (R_*/R_{\odot}) and luminosity (L_*/L_{\odot}). These values were then used to interpolate atmospheric spectra for flux ($\text{ergs s}^{-1} \text{cm}^{-2} \text{\AA}^{-1}$) from 1200 to 2×10^7 Å. The spectra were subsequently resampled onto 200 logarithmically spaced points. Careful inspection ensured that no spectral features were removed during resampling. The stellar interior models used for this study are the ‘DUSTY00’ models of Chabrier et al. (2000) combined with the ‘AMES-Dusty’, atmospheric models of Chabrier et al. (2000), which are all available online². For our T_{eff} range of $\approx 3000 \text{ K} < T_{\text{eff}} < 1600 \text{ K}$ the AMES-Dusty atmospheres are the most applicable (2700 K $> T_{\text{eff}} > 1700$ K). We did try including dynamic application of atmospheres based on the derived T_{eff} , i.e. using AMES-Cond for $T_{\text{eff}} < 1700$ K, but this resulted in large discontinuities between the model atmospheres and resulting spectra. Additionally, for the higher temperatures in our range, Martín et al. (2000) have found the NextGen models to be more applicable for $\sim T_{\text{eff}} > 2300$ K. However, as with the lower boundary this only applies to the edge of our temperature range and we feel it is better to use a consistent set of atmosphere and interior models across our grid. Since this only affects stars at the very edge of our temperature range, i.e. for the oldest and lowest mass objects (for the AMES-Cond case), we have adopted the AMES-Dusty models throughout.

2.1.2 Accretion flux

We assumed blackbody emission for the accretion flux. The selected accretion rate was used to derive an accretion luminosity (L_{acc}), where the material was modelled as free-falling from the disc inner edge onto the surface of the star. L_{acc} is calculated according to,

$$L_{\text{acc}} = \frac{GM_*\dot{M}}{R_*} \left(1 - \frac{R_*}{R_{\text{inner}}}\right), \quad (1)$$

where M_* is the stellar mass, \dot{M} the mass accretion rate, R_* the stellar radius and R_{inner} the radius of the disc inner boundary.

¹ http://www.astro.ex.ac.uk/research/bd_disc

² <http://perso.ens-lyon.fr/france.allard/>

The initial inner disc radius was set to be the co-rotation radius (this is discussed in more detail in Section 2.1.3). During the radiative transfer simulations of the disc the final inner dust-disc radius may be beyond the co-rotation radius due to dust sublimation effects (see Sections 2.2.2 and 4.1.2 for an explanation). Once the accretion luminosity was derived, an adopted areal coverage (A), over the stellar surface, was used to calculate an effective temperature (T_{acc}), for the accretion ‘hot’ spot, where

$$T_{\text{acc}} = \left(\frac{L_{\text{acc}}}{4\pi R_*^2 \sigma A} \right)^{\frac{1}{4}}. \quad (2)$$

Finally, a blackbody flux distribution is generated at T_{acc} and added onto the intrinsic stellar photospheric flux. In general, one would expect this to be an overestimate of the accretion flux, as for BDs large convective zones are expected on the stellar surface, and some of the accretion energy may act to further drive these convective currents, meaning flux is lost. It is worth noting however that observationally UV excesses are often used to recreate and then subtract an assumed accretion flux using a blackbody flux curve, which is essentially the reverse of this method.

2.1.3 Disc parameters

In this study we assume that accretion from the central star occurs along magnetically channelled columns from the inner disc boundary. For CTTS stars, Bouvier et al. (2007) show that the magnetic truncation radius (R_{mag}) is less than the co-rotation radius (R_{co}), where the angular Keplerian velocity of the disc is equal to the surface angular velocity of the central star. Calculations of the magnetic truncation radius depend on derivations of the surface magnetic field (Koenigl 1991). This is currently unavailable for BDs, due to an increased number of molecular species obscuring the Zeeman splitting signatures that are normally used to derive stellar surface magnetic fields. Therefore, for our model grid we have adopted an initial inner disc radius as the co-rotation radius,

$$R_{\text{inner}} = \left(\frac{GM_*\tau^2}{4\pi^2} \right)^{\frac{1}{3}}, \quad (3)$$

where τ is the stellar rotation period and R_{inner} is the inner radius. This is effectively adopting a disc-locking mechanism (without associated angular momentum loss), as for disc-locked stars, $R_{\text{mag}} \approx R_{\text{co}}$, (Koenigl 1991; Shu et al. 1994). Therefore, for our model simulations, this inner edge radius is dependent on, and derived from, the adopted value of the rotational period for the central star, as well as being weakly dependent on the stellar mass. As discussed in Section 1, the inner disc can be cleared through a number of mechanisms, including binarity or giant planet formation, photoevaporation or photoionisation of the disc and dust grain growth or settling. For BDD systems where a disc is modeled a treatment of dust sublimation is included (discussed in Section 2.2.2). However, the effects of binarity or giant planet formation are neglected. Further to the stellar mass and period required prior to calculation of the inner disc radius, we require a disc mass (in stellar masses).

Although we solve for the vertical disc structure, the radial structure of the disc is a free parameter. We assume that the surface density varies as $\Sigma(r) \propto r^{-1}$.

For this work the disc outer edge was set at 300 AU, this was chosen as a maximum size of the circumstellar disc. Bouy et al. (2008) have shown that the disc outer radius has little effect on the resulting SED. However, in our subsequent paper we will include models for outer radii of 100 AU and plan to extend this parameter range further to smaller values of the outer radius in the future.

2.1.4 Naked and disc systems

The combined (accretion plus photosphere) SED is then used as a boundary condition for the TORUS radiative transfer code and as a benchmark set of SEDs to model ‘naked’ BD systems. The set of ‘naked’ photospheres (plus accretion) are diluted by the factor $(R_*/\text{distance})^2$ to a distance of 10 pc. The ‘negligibly’ accreting, ‘naked’ stars can be used to produce absolute magnitude (and intrinsic colour) isochrones for comparison. The remainder are used to model systems showing active accretion where no disc is detected. For instance, Kennedy & Kenyon (2009) find 43 stars within their sample are actively accreting whilst no disc is detected (out of a total sample of 1253).

In summary the key required input variables to setup the model grid are as follows: stellar age and mass (which are used to derive the stellar flux) and accretion rate, areal coverage and rotation period (which are used to determine the the accretion flux and temperature). The disc parameters are set by a disc mass (expressed as a fraction of the BD mass), and a power-law distribution for the disc surface density.

2.2 Radiative transfer code: TORUS

We have used the TORUS radiative transfer code which was originally described by Harries (2000) and was subsequently updated by Harries et al. (2004) and Kurosawa et al. (2004). TORUS uses the method of Lucy (1999) to solve radiative equilibrium on an AMR mesh. The code also self-consistently solves the equation of vertical hydrostatic equilibrium and dust sublimation for the disc (described in Tannirkulam et al. 2007). The TORUS code has been extensively benchmarked (for radiative transfer in discs against Pinte et al. 2009).

2.2.1 Dust Size distribution

We have adopted a similar dust model to Wood et al. (2002) with the size distribution of dust particle given by

$$n(a)da = C_i a^{-q} \times \exp^{[-(a/a_c)^p]} da \quad (4)$$

where $n(a)da$ is the number of particles of size a (within the increment da), a_c is the characteristic particle size, with p and q simply used to control the shape of the distribution. C_i controls the relative abundance of each constituent species (i) in the dust. Wood et al. (2002) found that simulated SEDs fit observed SEDs better using this adjusted size distribution for the dust particles, as opposed to a simple power law. The best fitting values found in Wood et al.

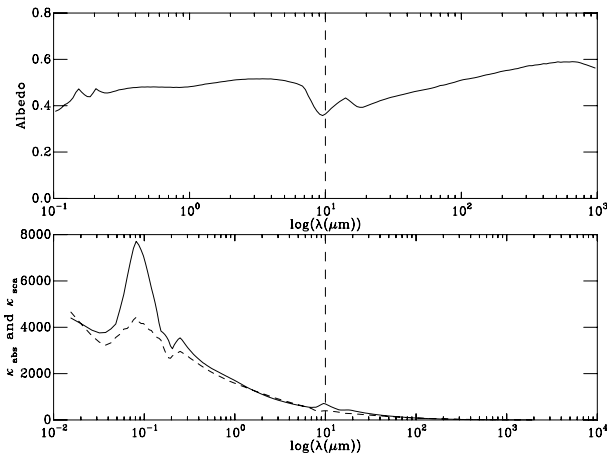


Figure 1. Figures of the albedo (top panel), and scattering (dashed line) and absorption (solid line) opacities (bottom panel) against $\log(\lambda)$ (in μm) for our adopted dust population. For both panels the vertical dashed line is plotted at $10 \mu\text{m}$ to highlight the silicate features.

(2002) were $q = 3.0$, $p = 0.6$ with $a_c = 50 \mu\text{m}$, also with an associated maximum and minimum grain size of $a_{\min} = 5 \text{ nm}$ and $a_{\max} = 1 \text{ mm}$. A slightly steeper power law dependence, with $q = 3.5$ (corresponding to the canonical MRN distribution) is more widely adopted (Bouy et al. 2008; Morrow et al. 2008; Pascucci et al. 2008). Here we have adopted the values of Wood et al. (2002) except for the parameter q where we have used $q = 3.5$. Wood et al. (2002) calculated the C_i values for amorphous carbon and silicon by requiring the dust to deplete a solar abundance of either component completely (using abundances from Anders & Grevesse 1989; Noels & Grevesse 1993). We have set $C_i = 1$ and adjusted the species using a grain fractional abundance (an equivalent process to that of Wood et al. 2002), however we have adjusted these grain fractions using the updated solar abundances of Asplund et al. (2006). The resulting difference in opacity between grain fractions matching the work of Wood et al. (2002) and the new grain fractions is only a slight enhancement of the silicate feature (due to the relative abundance of silicon increasing) which has little effect on the resulting SEDs. Figure 1 shows the resulting albedo, and scattering and absorption opacities, for our dust population, with a the vertical dashed line showing $10 \mu\text{m}$.

2.2.2 Dust sublimation and the inner disc edge

As our models assume magnetic truncation at the co-rotation radius, we have generated an inner hole. This also means that the disc will have an inner wall at this radius. Evidence for inner walls in circumstellar discs is apparent from the SEDs of disc systems, where a peak in emission is found between 2 and $3 \mu\text{m}$. The temperatures reached by such inner walls are expected to generate thermal flux contributions within this wavelength range (Dullemond et al. 2001). The circumstellar disc receives direct photospheric radiation and is strongly heated. This leads to an increased scaleheight, or ‘puffing up’ of the inner disc rim, and subsequent shadowing of the region immediately beyond it (Dullemond et al. 2001). The density-dependent nature of the dust sublima-

tion temperature (Pollack et al. 1994) may also play a role in shaping the inner rim (Isella & Natta 2005; Tannirkulam et al. 2007)³.

For low-luminosity systems the dust sublimation radius (R_{sub}) will be coincident with the co-rotation radius. However should the combined photospheric and accretion luminosities be sufficient the inner disc will be heated sufficiently that the dust close to the co-rotation radius will be sublimated, and we must account for this in our models. Furthermore, since the dust sublimation temperature has a density dependence (Pollack et al. 1994), it is both the location and shape of the inner wall that can change (Isella & Natta 2005; Tannirkulam et al. 2007).

Our treatment of dust sublimation is similar to that detailed in Tannirkulam et al. (2007), but with some enhancements to ensure a swift convergence of the sublimated rim. The dust sublimation proceeds as follows: An initial temperature distribution is found for the optically-thin limit by setting the global dust-to-gas ratio to a tiny value. Subsequent radiative equilibrium iterations are performed using the adopted dust-to-gas ratio of 0.01, but limiting the maximum optical depth across a given cell to τ_{\max} . Cells whose temperature exceeds the local dust sublimation temperature have their dust-to-gas ratio set to zero. Radiative equilibrium iterations and sublimation sweeps are performed at $\tau_{\max} = 0.1$, 1, and 10, with a final iteration of $\tau_{\max} = \infty$. Adequately solving the radiative-equilibrium necessitates resolving the disc’s effective photosphere, and adaptive mesh refinement is used to split the grid at the optically-thin/optically-thick boundary in order that the maximum cell size at this boundary is < 1 at a wavelength of 5500 \AA . Once a self-consistent sublimated rim has been determined, the equation of hydrostatic equilibrium is solved throughout the disc, and the sublimation iterations are restarted (the change in the density structure from the hydrostatic equilibrium step naturally feeds back into the shape of the inner rim). Five hydrostatic equilibrium steps are performed to ensure convergence, although a stable disc structure is normally found after three such iterations. For a more sophisticated, and chemically more complex, study of dust sublimation albeit for higher mass objects see Kama et al. (2009).

For our model grid the gas population is assumed to be essentially static with a zero optical depth.

2.2.3 SEDs

Once the radiative transfer code was completed simulated SEDs were generated. These SEDs can be generated for any distance and for any system inclination. For our models we have set the distance, to 10 pc to create absolute flux SEDs and selected ten inclinations equi-spaced in $\cos i$ (where $i=0, 27, 39, 48, 56, 64, 71, 77, 84$ and 90°). A further useful feature of the TORUS code is that the emitted photon packets which contribute to the SED are tagged on their way

³ Although we recognise that the inner hole in protostellar discs may be the result of giant planet formation or photoevaporation (Dahm & Carpenter 2009; Najita et al. 2007), these two mechanisms should result in a negligible mass-accretion rate (Dahm & Carpenter 2009) and therefore would represent a distinct evolutionary state of brown dwarf disc (BDD) systems to that of the CTTS-like phase we are considering here.

to the observer. These tags separate the packets into four groups. Firstly, packets are separated by source into thermal (disc) or stellar groups. These groups are then subdivided into those which reach the observer either directly or after scattering. The resulting SEDs are discussed in Section 2.2.3.

2.3 Photometric systems and derived quantities

Many observational studies use non-spectroscopic data to derive the pertinent parameters. Therefore in order to examine the practical effects in the ‘observational plane’ we have used the SEDs to produce broadband photometric magnitudes and subsequently colours. Broadband magnitudes were also derived in a large range of other filter sets not used explicitly in the analysis within this paper. These magnitudes are available online⁴ and are briefly discussed in Appendix A. In addition, monochromatic fluxes have been derived for all filters, and again are available online and discussed in Appendix A.

In order to derive broadband photometric magnitudes and colours the SEDs of either the disc or naked systems were folded through the filter responses of the required photometric system. As the fluxes in all cases are absolute, derived for an observer to object distance of 10 pc, no conversion is required to derive absolute magnitudes and therefore intrinsic colours.

We have integrated, the fluxes, using photon-counting and calibrated using a Vega spectrum for magnitudes in the optical and near-IR regimes. The filter bandpasses selected are, the optical system of Bessell et al. (1998) for *UBVRI* and the *CIT* system of Elias et al. (1982); Stephens & Leggett (2004) for *JHK*, with the required shift of $-0.015\text{ }\mu\text{m}$ as prescribed by Stephens & Leggett (2004).

We have also derived magnitudes in the mid-IR range using the IRAC and MIPS systems of the *Spitzer* space telescope. These magnitudes were derived using a conversion of flux to Data Number (DN) and calibrated using zero points derived from the zero magnitude fluxes published in the IRAC handbook⁵ and the MIPS instrument calibration website⁶.

We have chosen these specific filter due to their ubiquitous use and suitability for the derivation of the key stellar parameters of age, mass and, for populations, disc fractions. Therefore, by studying the changes of magnitudes (and colours) in these photometric systems we can test the predicted effects on these derived parameters caused by changes in the input parameters of our model grid. The optical magnitudes *VI* are used to explore age-related effects of varying the parameter space. Flux in the *VI* bands is only minimally affected by accretion flux (Gullbring et al. 1998) and disc thermal flux (Hartmann 1998) and, additionally, in a *V, V-I* CMD, the reddening vector lies parallel to the pre-MS, minimising any age effect of extinction uncertainty, (for a full discussion see Mayne et al. 2007; Mayne & Naylor 2008). The near-IR passbands of *JHK* are most often used to derive stellar masses. This is as for pre-MS objects the

reddening vector, in for instance, a *J, J-K* CMD, is almost perpendicular to the isochrones. The direction of this vector acts to minimise the mass effect of extinction uncertainties (the *CIT* systems was chosen to match Chabrier et al. 2000). Finally, as is now well documented the *Spitzer* IRAC passbands provide the best data with which to unambiguously separate naked and star-disc systems (Luhman et al. 2005). In addition, at longer wavelengths, the MIPS instrument provides sensitivity to disc systems at much larger radii (or debris discs).

Once the model grid was completed several checks were performed to verify the consistency of our results. For each individual model these checks were passed to our satisfaction before publication. Some problems remain, and these are explained in Appendix B.

3 PARAMETER SPACE

This section details the range of each of the input parameters we have varied and, where possible, gives justification for the selected ranges from published observations. The simulations in this paper cover variations in the stellar mass, stellar age, stellar rotation rate, accretion rate, the areal coverage of the accretion stream, disc mass fraction and the system inclination. A summary of the values adopted for each input variable is shown in Table 1.

3.1 Mass

Representative masses within the BD regime were chosen as follows: 0.01, 0.02, 0.03, 0.04, 0.05, 0.06, 0.07 & 0.08 M_{\odot} .

3.2 Age

Typical disc lifetimes for solar type stars are of order 10 Myrs (Haisch et al. 2001). Therefore, we have adopted input ages of 1 and 10 Myrs for our model grid, to span the approximate range of ages over which the discs influence will be important.

3.3 Rotation rate

Data for rotation rates, from periodic variability surveys, are widely available for a range of different age clusters of TTS. However, fewer studies exist on the rotation rates of BD mass objects. Rotation period data for σ Ori, at an age of ≈ 3 Myrs (Mayne & Naylor 2008), was studied by Scholz & Eislöffel (2004), where periods are found over the range 5.78–74.4 hours (≈ 0.24 –3.1 days) for BD mass objects. Scholz & Eislöffel (2005) study rotation period data for stars in the vicinity of ϵ Ori, with an assumed age of ≈ 3 Myrs (Zapatero Osorio et al. 2002) and the ONC at an age of ≈ 2 Myrs (Mayne & Naylor 2008). Rotation periods, from photometric variability, in the range 4.7–87.6 hours (≈ 0.2 –3.65 days) for BD mass stars are found. Joergens et al. (2003) study the rotational periods of BD (and very low mass stars) in the Chameleon I region. This region is ≤ 1 Myrs old, and the authors find rotation periods of 2.19, 3.376 and 3.21 days for their BD targets.

In some cases the periodic variability is irregular and assumed to come from active accretion hot spots on the BD

⁴ http://www.astro.ex.ac.uk/research/bd_disc

⁵ <http://ssc.spitzer.caltech.edu/documents/som/som8.0.irac.pdf>

⁶ <http://ssc.spitzer.caltech.edu/mips/calib/>

surface (see Bouvier et al. 1995; Herbst et al. 2007, for a discussion of variability causes), indicative of active accretion. All the studies mentioned infer a disc locking mechanism. Furthermore, Scholz & Eislöffel (2004) and Scholz & Eislöffel (2005) find evidence for a mass \propto period relationship extending into the BD regime. Additionally, Joergens et al. (2003) propose a shorter lifetime of ≈ 5 Myrs for BD discs, inferred from a shorter derived disc-locking timescale. However, as discussed in the previous studies, an imperfect disc locking mechanisms is also hypothesised as responsible for the less significant loss in angular momentum out to ages of 10 Myrs, for BD discs. The data on BD rotation rates, disc presence and disc locking are summarised and discussed in Herbst et al. (2007).

Therefore, to create a set of useful models to help contextualise the observational constraints for study of disc locking mechanisms, we must adopt a realistic and bounding range of rotation rates. For our model grid, and associated age range (<10 Myrs), we have selected 0.5 and 5 days. With the limits set at at the approximate median of faster rotators and the edge of the slower rotators.

3.4 Areal Coverage

As discussed in Section 3.3 evidence for irregular periodic variability has been found in BDs with detections of associated stellar discs. This is construed as evidence for accretion hot spots formed as magnetically channeled material hits the stellar surface (see discussion in Bouvier et al. 1995; Herbst et al. 2007). The irregularity is thought to be caused by changes in the magnetospheric structure and accretion rate (Bouvier et al. 1995). For our model we have assumed that disc material is disrupted at the co-rotation radius and channeled onto the star in the form of accretion hot spots with a characteristic temperature. Therefore, to calculate the characteristic temperature and the resulting blackbody accretion flux we must adopt an accretion rate and areal coverage of the accretion stream.

Little observational evidence can be found for approximate sizes of accretion hot spots due to their more transient nature and often smaller coverages, when compared to cooler or ‘plage’ spots (Herbst et al. 2007). Bouvier et al. (1995) modeled the size of the cool spots on solar-type stars for a selection of periodically variable candidates. They found projections of cooler spots, onto the stellar disc, of a few to $\sim 60\%$. Bouvier et al. (1995) also found projected sizes, onto the stellar disc, of typically a few % to around 10% for hot spots. Bertout et al. (1996) used observations of YY Orionis monitoring flux amplitude variations as a function of wavelength to derive a probable hot spot area of around 10%. The spot temperature was also modeled for YY Orionis in Bertout et al. (1996), resulting in a best fitting areal coverage of 11%. Therefore, to bound the probable areal coverage range of the accretion hot spots we have adopted areal coverages of 1 and 10%.

3.5 Accretion Rate

Accretion rates derived for pre-MS stars are of order $\log \dot{M} = -6$ to -11 (Natta et al. 2006), with the largest accretion rates found in so-called FU Orionis type objects. For the

more typical accretion rates ($\dot{M} = 10^{-11}$ to $10^{-8.9} M_{\odot} \text{yr}^{-1}$, for TTS, Dahm & Carpenter 2009), several studies have now suggested that the accretion rate is strongly correlated with the mass of the central star. This relationship was first suggested by Muzerolle et al. (2003) using various accretion diagnostics. Later, Muzerolle et al. (2005) derived a relationship of approximately $\dot{M} \propto M_*^2$. Further evidence was put forward by Natta et al. (2004), where accretion rates as low as $5 \times 10^{-12} M_{\odot} \text{yr}^{-1}$ were found for BDs. More recently, even lower accretion rates of $\approx 10^{-13} M_{\odot} \text{yr}^{-1}$, have been derived for BDs by Herczeg et al. (2009). Further support for a dependence of accretion rate on stellar mass was apparent in the significantly more homogeneous dataset of Natta et al. (2006). Natta et al. (2006) analysed a set of accretion rates and masses derived for BDs in ρ Ophiuchi and compared these results to stars in Taurus. They found that the accretion rate scales with central object mass into the BD regime, although with significant scatter.

As the relationship $\dot{M} \propto M_*^2$ predicts lower accretion rates for BD mass objects it is essential that we model systems at higher accretion rates, which may have been missed in current observational studies. Therefore, we have adopted accretion rates of $\log \dot{M} = -6, -7, -8, -9, -10, -11 \& -12$.

3.6 Disc Mass

Previously studies modeling BD discs have adopted a range of disc mass fractions, for instance (Walker et al. 2004) use 0.1, 0.01 and $0.001 M_*$. Wood et al. (2002) fitted observed spectra with modeled SEDs to derive a disc mass of $0.003 M_*$ for HH 30 IRS. Subsequent derivations of disc masses have converged to within an order of magnitude, with the following specific results: $0.03 M_*$ (ρ Ophiuchi, Natta et al. 2002), $0.055 M_*$ (GM Aurigae, Rice et al. 2003), $0.03 M_*$ (GY 5, GY 11, and GY 310, Mohanty et al. 2004) and $0.022 M_*$ (2MASS J04442713+2512164, Bouy et al. 2008). As the derived disc masses all have a similar order of magnitude we have adopted $M_{\text{disc}} \approx 0.01 M_*$. As changes in disc masses are expected to change the resulting SED less than perhaps, accretion rate for example, we have not varied the disc mass for this study. The results of simulations varying this parameter will be published in a future paper.

3.7 Inclination

Discs around BDs exhibit increased flaring, due to the reduced surface gravity in the disc (Walker et al. 2004). This increased flaring, and therefore larger scaleheight of the disc results in obscuration on the star at lower inclinations, when compared to higher mass stars and their circumstellar discs. As has been shown in Walker et al. (2004) effects caused by variations in the system inclination angle are much more significant for BDD systems, again compared to their higher mass analogues. Therefore, we have simulated ten observer to system inclination angles spaced evenly in $\cos i$ space, namely, 0, 27, 39, 48, 56, 64, 71, 77, 84 and 90° .

A final list of all varied parameters and their values can be seen in Table 1.

Input parameter	Values (# of values)
Mass (M_{\odot})	0.01, 0.02, 0.03, 0.04, 0.05, 0.06, 0.07 & 0.08 (8)
Age (Myr)	1 & 10 (2)
Rotation period (days)	0.5 & 5 (2)
Areal coverage (of \dot{M} , %)	1 & 10 (2)
Accretion rate ($\log(\frac{\dot{M}}{M_{\odot}} \text{yr}^{-1})$)	-6, -7, -8, -9, -10, -11 & -12 (7)
Disc mass (M_{*})	0.01 (1)
Surface density profile	r^{-1} (1)
Inclination (°)	0, 27, 39, 48, 56, 64, 71, 77, 84 & 90 (10)

Table 1. List of all varied input parameters. Resulting in a total number of models of 448 (plus 40 models without radiative transfer simulations for the naked BDs) and 4480 SEDs (plus 40 for naked BDs).

4 RESULT AND ANALYSIS

In this section we first discuss the physical structure, both density and temperature, of the BDD disc systems (Section 4.1) across our parameter space. Then we discuss the resulting simulated observations in Section 4.2. We present analysis in terms of the impacts of the disc structure on the SEDs and colours and magnitudes. Then in Section 4.3 we examine the reliability of age, mass and disc fraction derivation when applied to our model grid. In particular we discuss selection effects causing higher accreting systems to be unlikely to be classified as BDD systems. Essentially, despite not intrinsically including a dependence of accretion rate on stellar mass in our grid, we show that current observational techniques and theoretical models, applied to the grid ,would result in a relationship of this type being derived.

4.1 Disc Structure

The disc surface density is conserved in the initial density structure, $\Sigma^{\beta-\alpha}$. The initial scaleheight (h) and density (ρ) follow $h = h_0(r/R_*)^{\beta}\rho = \rho_0 \frac{R_*}{r} \exp(-\frac{1}{2}[z/h(r)]^2)$ respectively., where r and z are the radial and vertical coordinates. The initial values of α and β were 2.1 and 1.1 respectively. The values for α and β were chosen to optimise resolution of the vertically evolving disc, but minor variations are largely inconsequential as the systems evolves from this state. In our models we have, however, placed the inner disc edge at the co-rotation radius, as opposed to the dust destruction radius used in Walker et al. (2004). The initial disc scaleheight at 100 AU, $h(100)$, was set to 25 AU. As the simulation used vertical hydrostatic equilibrium and dust sublimation, both the disc scaleheight and inner edge location then evolved in the systems dependent on the input parameters. In this section we discuss the structure of the discs in terms of these two generated characteristics, i.e the disc scaleheight and inner edge location.

4.1.1 Disc Flaring

We have previously tested the results of the TORUS code against that used by Walker and co-workers, using a CTTS disc model and simultaneously solving for radiative and hydrostatic equilibrium (but not employing dust sublimation). These tests showed excellent agreement in density and temperature structure, as well as in the resultant SEDs. The results of these tests were presented by Walker (2006). It

is therefore unsurprising that at negligible mass-accretion rates our disc structures are very similar to those present in Walker et al. (2004). Typical discs around CTTS stars have scaleheights at 100 AU of between $h(100)=10$ to 20 AU, whereas for BDD systems, $h(100)=20$ to 60 AU (for 0.08 and 0.01 M_{\odot} respectively). As the accretion rate increases the flux levels of the central star increase and lead to heating of the disc which in turn leads to vertical expansion. We found that levels of vertical flaring increased only marginally with accretion rate. Significant differences, more than >5 AU increase in $h(50)$, in the vertical structure were not apparent until the high accretion rates of $\log \dot{M} = -7$ and -6 . Figures 2(a) and 2(b) show the density structure ($\log \rho$) in the disc from radial distances of 0 to 50 AU for example systems ($M_{*} = 0.04M_{\odot}$, Age=1 Myrs, $\tau=5$ d and areal coverage=10%), with accretion rates of $\log \dot{M} = -12$ and -7 , respectively.

Walker et al. (2004) state that the degree of disc flaring depends on the disc temperature structure and the mass of the central star, with the disc scaleheight $h \propto (T_{\text{disc}}/M_{*})^{1/2}$ (Shakura & Sunyaev 1973). Recently however Ercolano et al. (2009) proposed that the flaring varied in the opposite sense with stellar mass, i.e. $h \propto M_{*}$. This suggestion was based on evidence from Allers et al. (2006), where SEDs for 17 systems in the mass range $6M_{\text{Jup}} < M_{*} < 350M_{\text{Jup}}$ were fit with flared or flat disc models. In general, Allers et al. (2006) find that lower mass objects achieve better fits with the flat disc models and higher mass objects with the flared discs.

The results of Allers et al. (2006) show that above a mass of $50M_{\text{Jup}}$ all objects (6/17) are better fit with flared discs. Whilst at masses below $50M_{\text{Jup}}$ only one object is better fit by the flared disc model, with the remaining objects (10/17) better fit with flat models. Whether this result is statistically significant enough to assert a $h \propto M_{*}$ is doubtful as the fitting process contains (presumably) two fixed scaleheight distributions. Therefore, for our study we continue to assume that our flared BDD systems will have larger characteristic scaleheights than typical CTTS systems.

A comparison of Figures 2(a) and 2(b) shows an increase in the scaleheight at 50 AU of >5 AU, as the accretion rate moves from $\log \dot{M}=-12$ to -7 . However, despite this small change with high levels of accretion our grid shows scaleheights comparable to the work of Walker et al. (2004) and as such result in similar consequences for the SEDs and photometric magnitudes. The effects of this flaring and the increase in flaring for very high accretion levels on SEDs

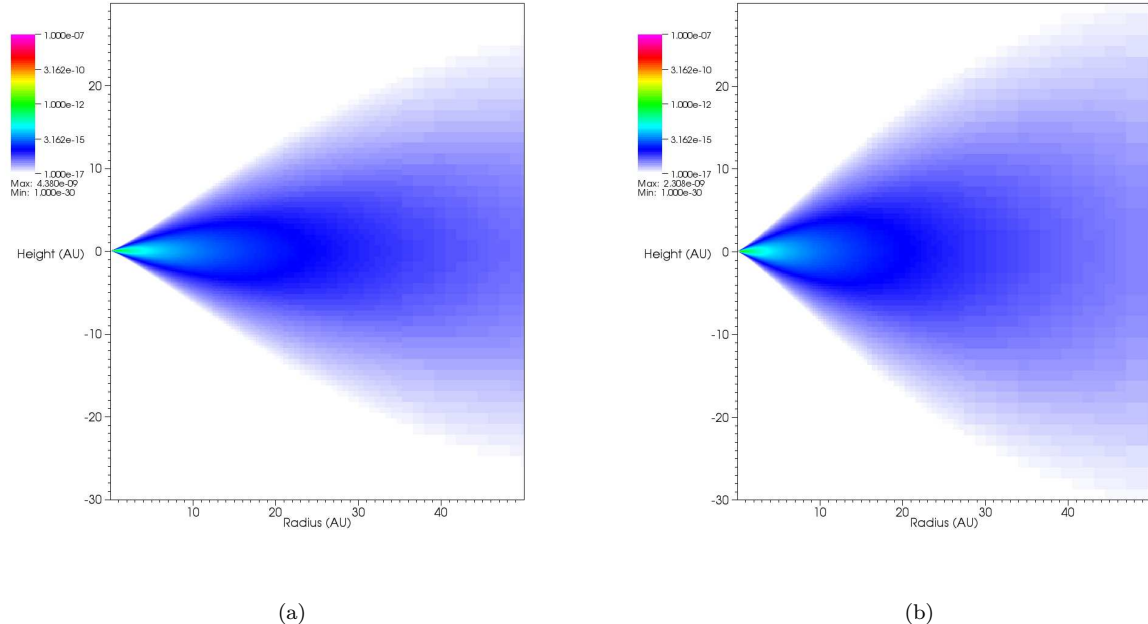


Figure 2. Figure showing the density structure ($\log \rho$) of the BDD system with $M_* = 0.04M_\odot$, Age=1 Myrs, $\tau=5$, areal coverage=10% and accretion rate of (a) $\log \dot{M}=-12$ and (b) $\log \dot{M}=-7$.

and photometric magnitudes are discussed in Sections 4.2 and 4.3 respectively.

4.1.2 Inner edge of the dust disc: location

The inner edge of the gas disc is fixed at the co-rotation radius, at which point the gas threads onto the magnetic field and follows the field lines in a funnel flow towards the protostellar surface. We make the assumption that the dust (should it exist at the co-rotation radius) is destroyed in the funnel flows. This is a reasonable assumption from both theoretical and observational perspectives: Radiative-transfer models indicate the temperature in the funnel flows may be very much greater than the dust sublimation temperature (> 10 kK, Muzerolle et al. 2003), while dusty funnel flows are likely to be optically thick in the visible regime, which would lead to substantial photometric variability as the funnels transit the photosphere—an effect that is unobserved.

Our models include a sophisticated treatment of dust sublimation (described in Section 2.2.2). As the flux levels of the central protostar increase with increasing accretion rates the flux incident on the inner edge increases and leads to increasing erosion of the inner edge of the dust disc.

As the inner edge moves, its temperature is expected to change. This has been predicted to lead to a correlation of inner edge position and IR excess (Meyer et al. 1997). This may act to bias surveys correlating rotation rates with IR excess to search for evidence of disc-locking. However, the flux from the inner edge will usually peak between 2 and $3\mu\text{m}$ (Dullemond et al. 2001), given that the dust sublimation temperature peaks at ≈ 1400 K for canonical densities. This means that for models where dust is significantly sublimated, the inner edge will *usually* have a temperature of

≈ 1400 K and this correlation of disc position and temperature will be lost (although see below).

Equation 3 shows that as the rotation period of the protostar increases the co-rotation radius decreases. This will result in, initially, shorter period systems having closer and hotter inner edges than their longer period counterparts. In addition, if the accretion rate is increased in these systems the incident flux on the inner wall will increase leading to a rise in the temperature of the inner edge. At some point the dust sublimation temperature may be reached, leading to a change in radial position of the wall. In addition, the temperature of the inner edge will then tend to the dust sublimation temperature.

A further complexity arises when one considers that the density of material in the disc falls with increasing radius from the star ($\rho(r) \propto r^{-\alpha}$), and that the dust sublimation temperature is density dependent (Pollack et al. 1994). Therefore, for systems where the inner edge has been eroded significantly from the co-rotation radius, the temperature of the inner edge will fall systematically as the inner dust disc radius increases.

For further analysis, and throughout the rest of this paper, we will separate the systems into two groups; those systems with $\log \dot{M} \leq -9$ and $\log \dot{M} > -9$, classed as typical and extreme accretors. This distinction is based on the point at which the systems undergo both significant sublimation ($\Delta R_{\text{inner}} > 1R_*$) and have an accretion luminosity that is comparable to the photospheric luminosity (see Section 4.2.1). In order to examine the effect of dust sublimation on our models we have measured the radius of the inner edge of the dust disc by integrating from the centre along the midplane until an optical depth of $2/3$ (at 5500\AA) is reached. Figure 3 shows the radial density distribution of the disc. In this case, the final inner edge radius, and there-

fore temperature, is no longer strongly correlated with the rotation rate. Figure 3 shows the final inner edge location (R_{inner}) against the temperature of the inner wall (T_{inner}). The left panel shows the systems designated as typical accretors and the right panel those with extreme accretion rates. For both panels the systems with rotation periods of 0.5 and 5 days are plotted in red and blue respectively. Those systems where the change in inner radius was greater than $1R_*$, classed as significantly sublimated, are plotted as crosses.

The left panel of Figure 3 shows that, taken as a whole, our models with typical accretion rates show a clear correlation between the temperature at the inner edge and the radius to this boundary. This agrees with the work of Meyer et al. (1997) where this correlation is found for there $R_{\text{inner}} = 1-12R_*$ and $\log \dot{M} = -9$ to -5 , for flat disc models. Meyer et al. (1997) use this correlation, and the derivation of IR magnitudes, to predict a relationship between IR excess and radius to the inner wall. Our data indicate that this correlation, for typically accreting systems will translate into a correlation between rotation rate and IR excess. This could have important implications for studies of disc-locking where disc presence is examined as a function of rotation rates, provide an intrinsic bias. In practice however, this correlation is weak (in fact unobservable) in our data due to the combined effects of the inner disc wall shape, inclination and flaring effects. This is discussed in more detail in Section 4.3.

Figure 3 shows that for those systems where significant disc erosion ($\Delta R_{\text{inner}} > 1R_*$) has occurred the resulting temperature of the inner edge is weakly correlated with the inner edge radius, but, critically, not correlated with rotation rate. The inner edge temperatures of the remaining systems for the extreme accretors are slightly anti-correlated with the radius to the inner edge. For the systems with typical accretion rates, and longer periods, Figure 3 shows there is again a weak correlation between the radius to, and the temperature of the inner edge. For the shorter period models with typical accretion rates there is no clear correlation between the temperature at the inner edge and radius to this edge.

4.1.3 Inner edge of the dust disc: shape

The initial shape of the inner edge of the dust disc is a vertical wall coincident with the co-rotation radius. In the previous section we have shown that models with a negligible accretion rate do not significantly sublimate the dust, and hence the edge remains vertical. This inner edge is heated by direct radiation from the protostar, and its scaleheight increases. Disc material behind the inner rim is shielded from direct radiation and has a smaller scaleheight, leading to the ‘puffed up’ inner rim predicted by Dullemond et al. (2001). This effect is illustrated in Figure 4(a), a model in which there is negligible dust sublimation.

As the flux of the central object increases significant dust sublimation occurs, leading to a change in the radial position of the dusty inner edge, but also shaping it: The density drops rapidly away from the midplane, and since the dust sublimation temperature also falls the edges of the inner dust disc become curved—this the mechanism described analytically by Isella & Natta (2005). We illustrate this effect in Figure 4(c), which also shows a scaleheight decrease

behind the curved inner rim, over a significantly larger radial scale than the previous model.

Finally the most extreme accretor (Figure 4(e)) shows dust being destroyed out to very large radii (~ 0.1 AU). A curved rim is present, without any obvious decrease in scaleheight behind the inner rim. The distance from the central object is such that the vertical component of gravity is much diminished, and the disc has a substantial scaleheight at the inner edge, meaning that it reprocesses significant protostellar radiation leading to a high near-IR excess.

We note that a similar sequence is apparent across the grid for set masses. However, the balance of the rotation period, and therefore inner edge location, and age and areal coverage, therefore flux levels, leads to changes in the accretion rate at which the dust sublimation starts. However, in almost all cases the dust sublimation does not become significant until at least $\log \dot{M} = -9$ (as discussed previously).

4.2 Observable Consequences of Disc Structure and Accretion

The resulting converged disc structures, as discussed in Section 2.2.3 are then used to create simulated SEDs and derive broadband photometric magnitudes. In this section we discuss the effects of accretion and disc presence on the simulated observations.

4.2.1 Accretion dominance

As $T_{\text{acc}} \rightarrow T_{\text{eff}}$, disentangling the accretion and stellar photospheric flux, in order to derive accretion rates becomes difficult. This equivalence in accretion hot spot and stellar photospheric temperature, for an accretion rate of $\log \dot{M} = -9$, occurs at a fractional coverages of 20 and 10%, for rotation periods of 5 and 0.5 days (with $M_* = 0.04M_\odot$ and an age of 1 Myr). Additionally, higher accretion rates can produce enough flux to ‘veil’ the underlying photospheric features, and significantly change the peak flux levels. Heavy veiling of atomic lines has been extensively observed in CTTS systems (e.g Kenyon & Hartmann 1995).

Figure 5 shows the effect of increasing the accretion blackbody flux (for increasing accretion rates) for a BD, $M = 0.04M_\odot$, at 1 Myr. Whilst the photon packets originating from the star (both from L_* and L_{acc}) will be tagged as stellar by TORUS, we can separate these flux contributions simply by observing the naked star system. The panels in Figure 5 show the flux from a naked system, with no treatment of the disc. This enables us to view the effect of increasing accretion rate on the photospheric flux in isolation. The accretion rates included in all panels are $\log \dot{M} = -8$, -9 and -12 (blue, black and red lines respectively). The bottom panels show the systems with a rotation period of 5 days and top panels for those with a rotation period of 0.5 days. Given our assumption that accretion occurs from the co-rotation radius, decreasing the rotational period moves this accretion radius closer to the star, $R_{\text{inner}} \propto \tau^{2/3}$ (see Equation 3). As the accretion radius moves further from the star the potential energy released by the accreted material is increased. This effect can be seen when comparing the top and bottom panels, although the effect is marginal for all but the highest displayed accretion rates.

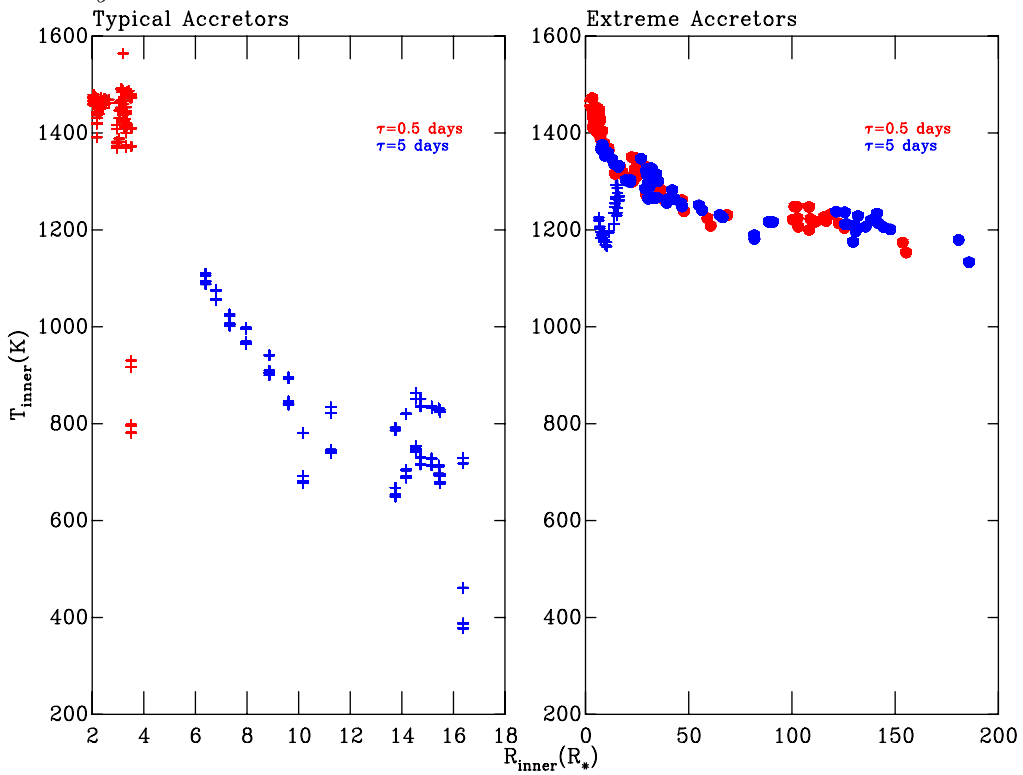


Figure 3. Figure showing data for the inner edge location (R_{inner} , R_*). The typical accretors are shown in the left panel and the extreme accretors in the right panel (see text for explanation). Both panels separate the systems by period, with those systems with rotation periods of 0.5 and 5 days shown as red and blue symbols respectively. In addition, systems where $\Delta R_{\text{inner}} < 1R_*$ are plotted as crosses and $\Delta R_{\text{inner}} > 1R_*$ as filled circles (this is only achieved by some systems classed as extreme accretors).

The left panels show accretion streams with an areal coverage of 10% and the left panels 1%. As the areal coverage reduces, the effective temperature of the accretion hot spot increases, resulting in an increase in accretion flux, and a shift to bluer wavelengths of the peak flux. This can be seen clearly by comparing the left and right panels of Figure 5. As the rotation rate increases the co-rotation radius also increases, as shown in Equation 3, $R_{\text{inner}} \propto \tau^{\frac{2}{3}}$. Therefore, as Equations 1 and 2 show $L_{\text{acc}} \propto 1 - \frac{R_*}{R_{\text{inner}}}$ and $T_{\text{acc}} \propto (L_{\text{acc}}/A)^{\frac{1}{4}}$, the temperature of the accretion hot spot increases as the rotational period increases. This is due to the increase in potential energy lost by the mass accreted. This can be seen by comparing the left and right panels of Figure 5. Perhaps the most important, albeit qualitative, result shown is Figure 5 is an insight into the accretion rate at which the accretion blackbody flux dominates over the photospheric flux. Figure 5 shows that as the accretion rate raises above $\log \dot{M} = -9$ for systems with 1 or 10% areal coverage, the accretion flux dominates the emergent SED at both periods. Effectively, the spectroscopic features of the photosphere are veiled by the additional continuum accretion flux. Therefore for reasonable coverages (1–10%) and rotational periods (0.5–5 days) the photospheric flux is effectively veiled by accretion flux for accretion rates $\log \dot{M} > -9$. It is also clear from Figure 5 that the magnitude becomes brighter and the colour bluer (in terms of optical photometry) with increasing accretion rates as expected (Gullbring et al. 1998). The impact on the photometry of BDD systems

is discussed in the next section for individual stars and in Section 4.3 for populations.

4.2.2 Flaring and the Inner Edge

As shown in Figures 2(a) and 2(b) and discussed in Section 4.1.1, BDD systems in vertical hydrostatic equilibrium have highly flared discs. As discussed in Walker et al. (2004) this increased flaring (when compared to CTTS stars) leads to occultation of the star at lower inclination angles and, therefore, significant changes to the SED. Increases in the inclination angle for these systems quickly lead to a significant proportion of the stellar flux being intercepted and reprocessed by the highly flared disc. This reprocessing will lead to a change in the flux levels at the shorter, bluer, wavelengths as more stellar flux is intercepted by the disc. It will also lead to significant changes in the flux reaching the observer from the inner and outer regions of the disc as the system approaches edge on. Also, as discussed in Section 4.1 the addition of dust sublimation leads to a change in the shape of the inner edge, where the temperature is sufficient. Figures 4(a), 4(c) and 4(e) show a range in inner edge shapes, from flat walls through concave to convex curves, caused by the radial density profile of the disc and the dependence of the sublimation temperature on density. This change in shape, as noted for Herbig Ae stars by Tannirkulam et al. (2007), will lead to changes in the characteristics of the SED, or derived IR excess, with inclination angle (Tannirkulam et al. 2007), for close to face on viewing angles.

Figure 6 shows the SEDs for the BDD system of Figures

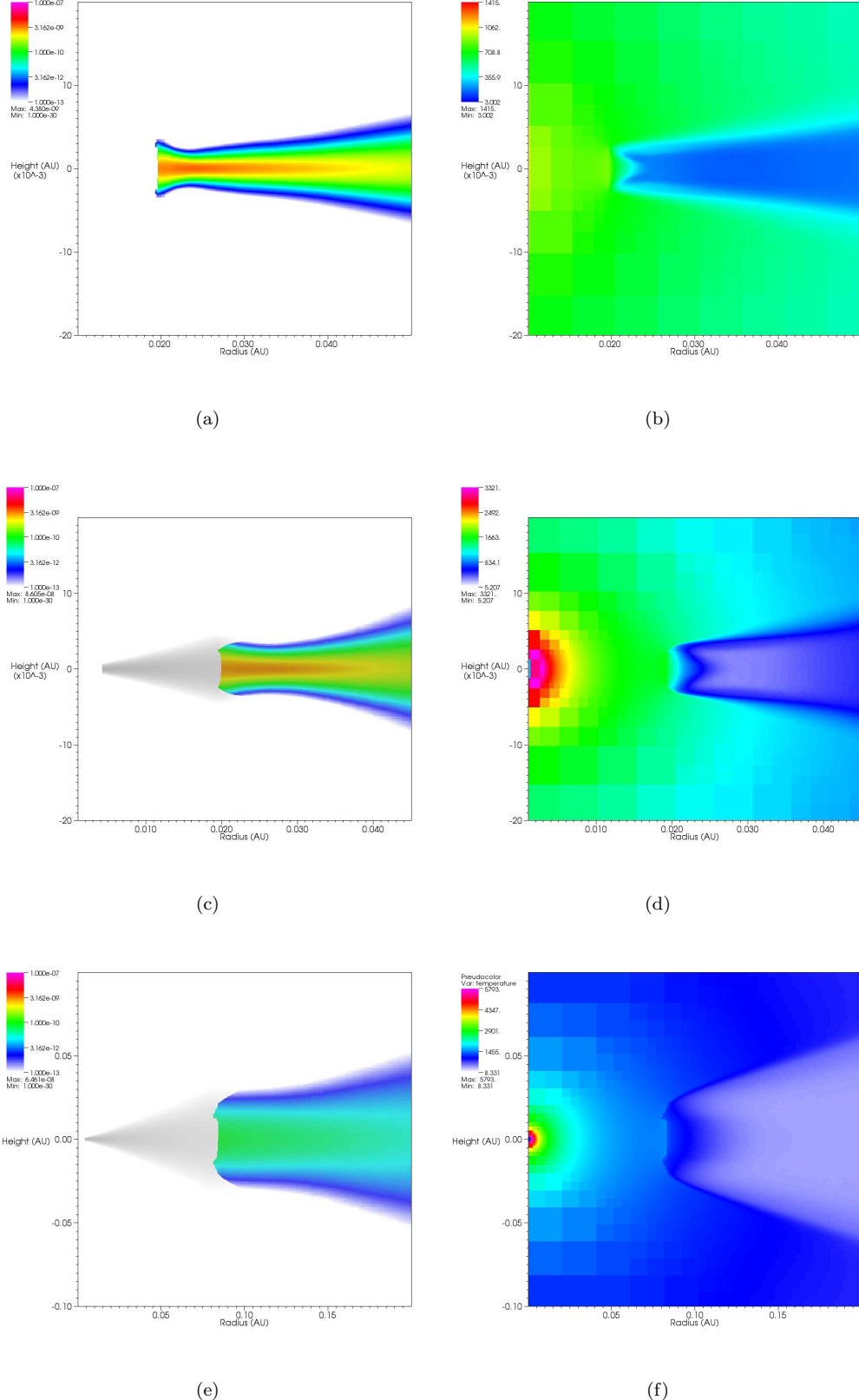


Figure 4. Figure showing both the initial (grey scale) final density ($\log \rho$) where dust is present (colour scale, left-hand panels) and temperature (right-hand panels). System parameters are: $M_* = 0.04 M_\odot$, Age=1 Myrs and areal coverage=10%, $\tau=5$ days and accretion rate $\log \dot{M}=-12$ (a, b); $M_* = 0.04 M_\odot$, Age=1 Myrs and areal coverage=10%, $\tau=0.5$ days and accretion rate $\log \dot{M}=-7$ (c, d); $M_* = 0.04 M_\odot$, Age=1 Myrs and areal coverage=10%, $\tau=0.5$ days and accretion rate $\log \dot{M}=-6$ (e, f).

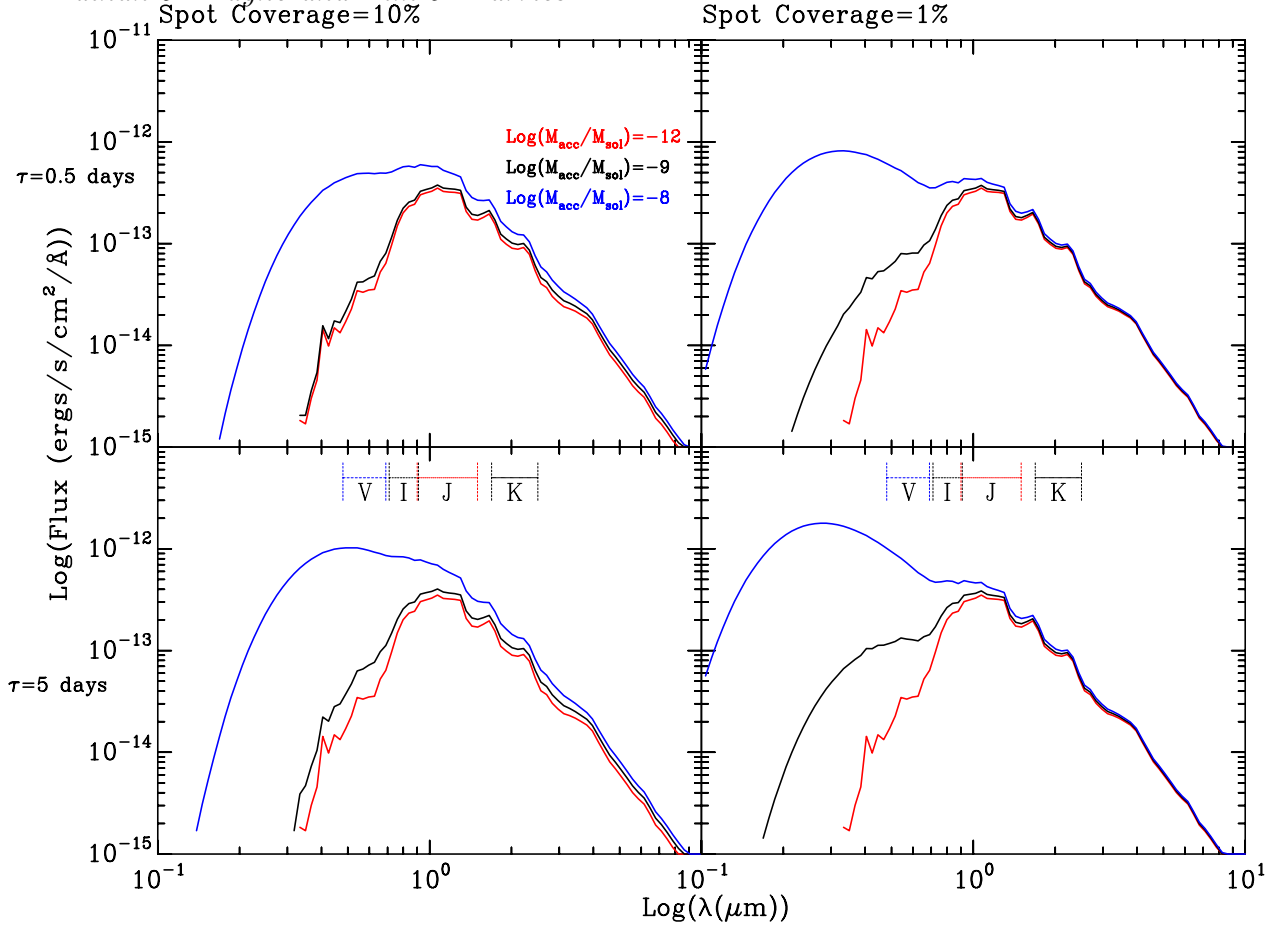


Figure 5. Figure showing the photospheric flux ($\log(\text{ergs/s/cm}^2/\text{\AA})$) against λ ($\log(\mu\text{m})$) of a BD with $M = 0.04M_\odot$, at 1 Myr. No disc is included, but blackbody fluxes from an accretion stream at the rates of $\log \dot{M} = -8, -9$ and -12 are shown as blue, black and red lines respectively. The bottom panels show accretion for a star rotating at 5 days, with the top panels showing that of 0.5 days. The left panels systems with an areal coverage of 10% and the right panels has 1%. The vertical and horizontal dashed lines (in the lower panels) denote the approximate sensitivity ranges of our chosen V, I, J and K filters.

2(a) and 2(b) as the top and bottom panels respectively. The lines show the flux over all the ten inclinations (see Table 1), with the dashed line showing the inclination at which a sharp fall in flux is seen. This inclination will be the angle at which the star and inner disc becomes obscured by the flared outer disc. These inclinations are 71° and 56° for $\log \dot{M} = -12$ and -7 respectively. This effectively means that for higher accretion rates a more significant fraction of the stars, in a given population, may have flux below a threshold detection limit.

The changes in flux with inclination will clearly lead to changes in the observed magnitudes and colours with inclination. Figure 7 shows the M_V and M_J magnitudes in the top and bottom panels respectively. The magnitudes are then marked as crosses as a function of inclination. The systems shown in both panels have an age of 1 Myr, mass of $0.04M_\odot$, rotation rates of 0.5 and an areal coverage of 10%. The systems with accretion rates of $\log \dot{M} = -12, -9$ and -7 are shown in black, red and blue, respectively. The panels also show the system with the highest accretion rate but with a rotation rate of 5 days as a dashed line. The vertical dotted lines in the lowest panel simply illustrate the inclinations of 71° and 56° .

Accretion flux was shown to dominate the underlying,

intrinsic, photospheric SED for accretion rates of $\log \dot{M} = -9$ (see Figure 5). As one would expect this leads to significant changes in the derived photometric magnitudes for bands blueward of a few microns, where the accretion and photospheric flux dominate. This is shown in the top panel of Figure 7. As the accretion rate increases, the system moves to brighter magnitudes in M_V . The move to brighter magnitudes becomes significant once the accretion rate exceeds $\log \dot{M} = -9$. Again moving from the fast to slow rotation period increases the potential energy released and in this case results in a brighter M_V magnitude. As one moves to longer wavelength photometric bands, as shown in the middle panel. The increase in accretion rate affects these magnitudes, i.e. M_J are less significantly affected. Figure 7 also shows the change in magnitude caused by obscuration from the flared outer disc. The occultation starts earlier for the higher accretion rates, with the magnitudes in M_V and M_J moving fainter at earlier inclinations for the higher accretion rates.

For our model grid the inner edge shape clearly changes with increasing flux levels and therefore accretion rate. This, for individual systems will lead to the reduced dependence of the IR colours on inclination as the edge moves from a vertical to a convex boundary as found by Isella & Natta (2005).

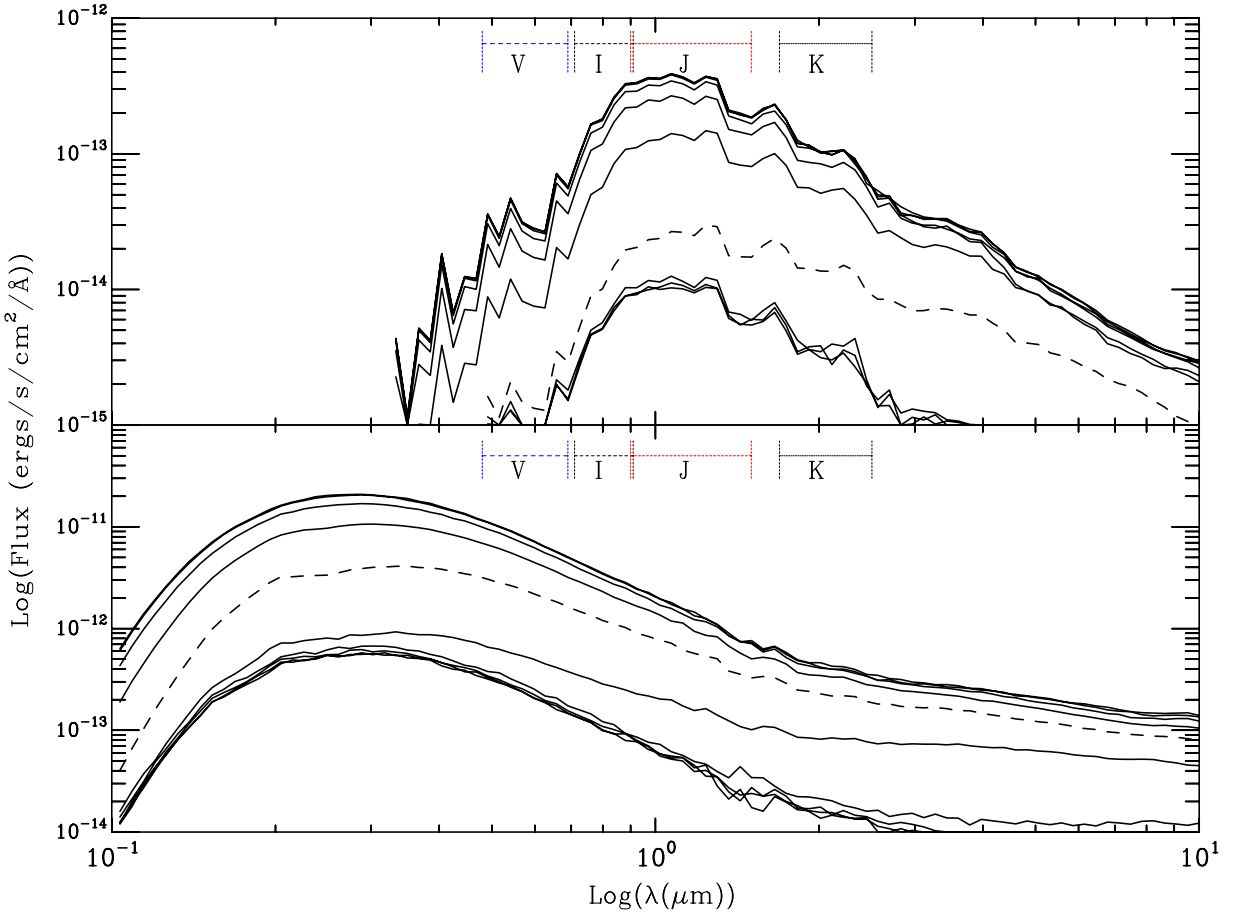


Figure 6. Figure showing both total SEDs of the systems shown in Figure 2(a) and 2(b) as the top and bottom panels respectively. The lines show the SEDs of all inclinations (see Table 1), with the obscuration angle shown as a dashed line, 71° and 56° for $\log \dot{M} = -12$ and -7 respectively.

Practically, for populations of stars however disentangling this effect from the influences of various other parameters (such as changing disc scaleheights and accretion rates) on the IR colours is difficult. Essentially, matching flux levels between two systems whilst maintaining a difference in inner wall shape is impossible.

Thus, for individual systems changes in the accretion rate and disc structure lead to significant changes in magnitudes and colours. The data presented in this section are for an isolated mass and age. However, the trends described are evident throughout our model grid for any given subset, and as such are representative. The scatter or changes in magnitude in the individual systems will change as a function of the remaining variables, but the dominant input variables affecting simulated photometry are accretion rate and inclination. For populations of stars these changes in magnitude and colour act to scatter or spread a BD locus in photometric space.

4.3 Parameter derivation

Practically, most parameters for young pre-MS and BDs are derived from surveys of populations, usually open clusters, using broadband photometry and subsequently constructed colour-magnitude and colour-colour diagrams (CMDs and

CoCoDs respectively, hereafter). In this section we explore the consequences of our model grid on the derivation of the primary parameters of age, mass and disc fractions, from populations. This in turn leads to highlighting selection effects with, for instance, the mass to accretion rate relation.

To delineate the effects of the accretion rate and circumstellar discs we have subdivided the grid into two groups (as discussed in Sections 4.1), those with accretion rates typical for higher mass CTTS objects, defined as $\log \dot{M} = -12$ (negligible) to $\log \dot{M} = -9$ and those with elevated accretion rates, where $\log \dot{M} > -9$. For several of the plots in this section the magnitude and colours for the $M_* = 0.01 M_\odot$ systems at high inclinations become extremely faint and red, and we omit them from the figures in order to conserve an appropriate scaling for the majority of the models. Additionally, stars at the highest inclinations, i.e. edge-on disc systems, are often omitted from the figures due to their extremely faint magnitudes, meaning they would not be practically observable.

As discussed in Section 4.1 the inner edge location is correlated with inner edge temperature (albeit differently for the typical and extreme accretors). As noted by Meyer et al. (1997) this could lead to a correlation of IR excess with inner edge position. As expected however, scatter caused by variations in inclination and disc structure act to remove this

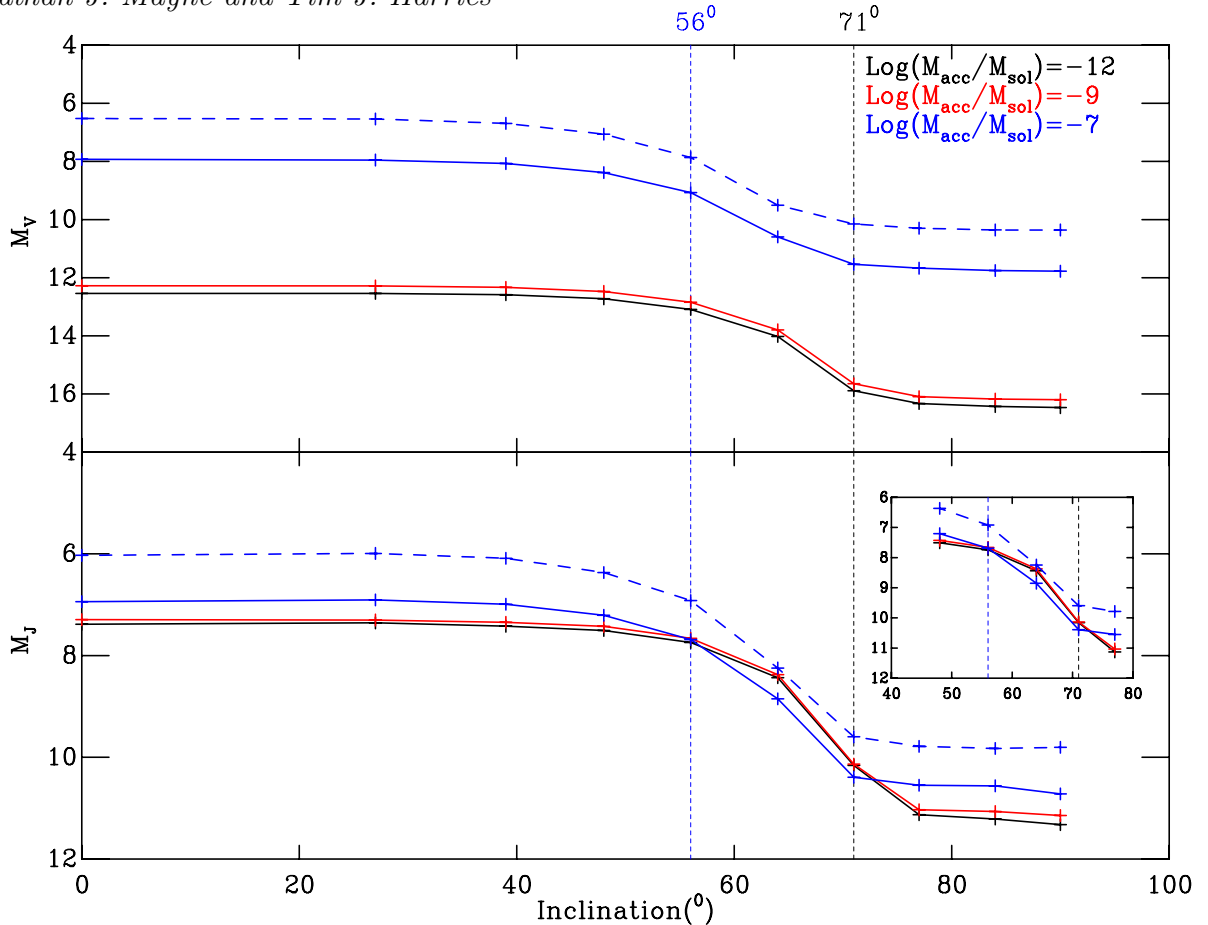


Figure 7. Figure showing M_V and M_J magnitudes as a function of inclination, shown as top, middle and lower panels respectively. The magnitudes of systems with $M_* = 0.04M_\odot$, an age of 1 Myr, areal coverage of 10% and rotation rate of 0.5 days are shown as solid lines (and crosses). The systems with accretion rates of $\log \dot{M} = -12, -9$ and -7 , are shown in black, red and blue respectively. The panels also show the systems with the highest accretion rate but for a rotation rate of 5 days, as dashed lines (and crosses). The vertical dotted lines show the inclinations of 71° and 56° . Finally, the inset panel simply shows a magnification of the region of interested for the M_J magnitude.

correlation for populations. The correlation for an individual set of a systems, i.e. all variables fixed except rotation rate, between IR colour and rotation rate is preserved. However, as shown in Section 4.1 the changes caused by accretion rate and inclination angle are the most significant, and act to remove any correlation between rotation rate and IR colours for populations. In fact, for our grid the simulated photometry shows no significant correlation between rotation rate and IR colours. The work of Meyer et al. (1997) studied flat accreting disc, therefore, as we have increased variation in disc structure by applying vertical hydrostatic equilibrium it would be interesting to see if any correlation appears for analytically defined disc structures. We have run a set of parallel models using analytical disc structures and will publish the results in a subsequent publication. Overall, as found in Walker et al. (2004), the dominant scattering effect for BD disc systems in an optical CMD appears to be caused by accretion rate and inclination. Therefore for derivation of parameters we explore the scatter in BD loci as a function of accretion rate and inclination.

4.3.1 Mass and Age Derivation

For the derivation of ages optical CMDs, in particular in V , $V-I$, are most often used, and indeed most suitable. Whereas, IR CMDs, such as a J , $J-K$ CMD, are most suitable for mass derivation (see references and discussions in Mayne et al. 2007; Mayne & Naylor 2008, and Section 2.3).

The use of pre-MS and BD isochrones for the derivation of single star parameters is at present not proven to be reliable (see discussion in Mayne & Naylor 2008). Practically, therefore, median ages are derived from populations. Subsequently, derived masses are still unreliable but at least based on a consistent age. This problem is being addressed by Bell et al. (in prep), where K band photometry and known eclipsing binaries are being used to refine pre-MS isochrones. In this section we plot the data for our 1 Myr systems only and explore the resulting scatters caused by the disc presence and accretion luminosity.

Figures 8 and 9 shows CMDs in M_V & $(V-I)_0$ and M_J & $(J-K)_0$ respectively. The left panels of both figures shows stars classed as typical accretors with accretion rates of $\log \dot{M} = -9, -10$ and -11 & -12 , shown as blue, black and red dots respectively in the top panels. The right panels of

Figures 8 and 9 show systems with extreme accretion rates, with $\log \dot{M} = -6, -7$ and -8 shown as blue, black and red dots respectively, in the top right panel. The bottom panels then show the systems separated into groups by inclination. These groups are $\theta \leq 48^\circ$ as blue dots (classed as face-on systems), $\theta > 56^\circ$ & 64° (classed as the expected systems, as the expectation value of $\cos(\theta) = 60^\circ$) as black dots and $\theta \geq 71^\circ$ (classed as edge-on systems) as red dots (for typical, bottom left, and extreme, bottom right accretion rates). The left panels then show naked stars isochrones (created from our grid of simulated photometry) for 1 Myrs at accretion rates of $\log \dot{M} = -12$ and -9 , as solid and dashed lines respectively (with coverage of 10% and rotation rates of 5 days). Whereas the left hand panels show naked stars isochrones of $\log \dot{M} = -6$ and -9 as solid and dashed black lines respectively (with coverage of 10% and rotation rates of 5 days). The solid green line, in the top panels, shows the 1 Myr isochrone of Siess et al. (2000) adjusted to a distance of 250 pc and an extinction of $A_V = 2$ mag, simulating a background population of CTTS stars.

As can be seen in Figures 8 and 9 current accretion and disc presence in a star and disc systems creates a scatter in our simulated photometry indicative of a much larger isochronal age or mass spread. Indeed, for many BDD systems even at nominal accretion rates of $\log \dot{M} = -11$ or -12 , for our simulations, the colours of these stars move significantly blueward of the expected BD locus in a $M_V, (V - I)_0$ CMD and redward in a $M_J, (J - K)_0$ CMD. As, in the case of typical accretors, the input variables are in the range expected for a BD population, one could reasonably expect observed true BD loci to show a similar scatter. It is clear that even a wide photometric selection would not even include all of the negligibly accreting systems at expected inclinations. Whilst the derivation of masses and ages for these objects will be difficult. Furthermore, for the higher accretion rates of $\log \dot{M} = -9$ or -10 the movement of the star within the CMD will effectively shift the star into the contamination region expected for background CTTS or MS stars at a $(V - I)_0$ of ≤ 1.5 and $M_V 12\text{--}10$, and as such the star would not be included in a photometrically selected BD sample. The solid green line, in the top panels of Figures 8 and 9, showing the 1 Myr isochrone of Siess et al. (2000) at a distance of 250 pc and extinction of $A_V = 2$ mags shows that the BDD systems with higher accretion rates could easily be confused for a background CTTS or MS population. Indeed misclassification of a BDD system as a CTTS system has already been revealed in White & Basri (2003). For the extreme accretors, as shown in the right panels of Figures 8 and 9, there is little chance of these objects being classed, photometrically, as BD candidates or being assigned the correct mass. Therefore, if one attempted to locate a population of BDD systems with elevated or extreme accretion rates, target selection would have to be placed at much brighter magnitudes, and bluer for optical or redder for IR, colours.

This scatter for both typical and extreme accretors is a strong function of inclination, where, as the inclination is increased the objects are pushed lower in the CMD. Indeed, for the edge on cases some objects have magnitudes fainter than those shown (for instance $M_V \approx 20$). This is expected as the star becomes obscured by the flared disc, interestingly for typical systems the bottom right panels show that this occurs for inclinations above around 71° (as found in Figure

6) in most cases. However, even for the lower inclination angles some objects have very faint magnitudes, this is due to the disc flaring leading to earlier obscuration of the star as discussed in Section 4.1. Crucially, the top panels show that the scatter from the isochrone is generally correlated with accretion rate. Effectively, as the accretion rate increases the BDD system moves farther away from the isochrone and is therefore less likely to be classified as a BDD system and included in any target samples of such objects. Overall, the dominant scattering effect for BDD systems in an optical CMD appears to be caused by accretion rate and inclination, and therefore obscuration effects of the disc on the star.

We have presented CMDs constructed using M_V , $(V - I)_0$ and M_J , $(J - K)_0$. The scatter and correlations of scatter with accretion rate and inclination found within these CMDs are however, representative of CMDs constructed using optical or near-IR colours and magnitudes.

If one adopts the range of input parameters we have used (see Section 3 for justification), our simulated photometry shows, qualitatively, that a coeval 1 Myr population of accreting BDs and BDD systems, with typical accretion rates and range of inclinations, will exhibit a significant scatter in apparent isochronal age. Furthermore, objects with typical (and extreme) accretion rates are scattered sufficiently in CMD space to prohibit their identification as BDs. Indeed, these objects would not be included in a photometrically selected sample of BDs, and as such are unlikely to be assigned the correct masses or ages. The scatter from the naked 1 Myr systems, generally, increases with increasing accretion rate. It is important to note at this point that these conclusions are qualitative, and obviously based on our assumptions. However, the repercussions for isochronal age derivation and sample selection in the BD regime could be profound. Indeed this study has only included the effects of current or ongoing accretion from a disc, it has neglected any effects of accretion, both past and present, on the evolution of the central star. This past accretion could also act to reduce the stars radius, accelerating contraction (Tout et al. 1999; Siess et al. 1999) and introducing additional scatter in a coeval population proportional to the range in accretion rates (see Mayne & Naylor 2008, for full discussion). In addition we have shown that the typical accretion rates may scatter BDD systems into the region of a CMD occupied by the CTTS or background MS locus.

The fact that scatter in the CMD increases with increasing accretion rate casts doubt on the veracity of the mass to accretion rate relationship. For our model grid we have not assumed any such relation, therefore, as our data would also show a similar relation it suggests that the observed result may be caused by intrinsic scattering. The relation $\dot{M} \propto M_*^2$ suggests that there is a dearth of lower mass stars accreting at higher rates. We have shown that for accretion rates in the range $\log \dot{M} = -12$ to -9 the BDD systems with higher accretion rates would be preferentially missed using photometric or isochronal selection. Furthermore, for the extreme accretors the BDD systems are scattered far from the non-accreting naked BD locus. This effectively means that applying standard photometric selection and considering possible dynamic magnitude ranges (to define saturation and magnitude limits), the systems with extreme accretion rates would not be classified as BDD systems.

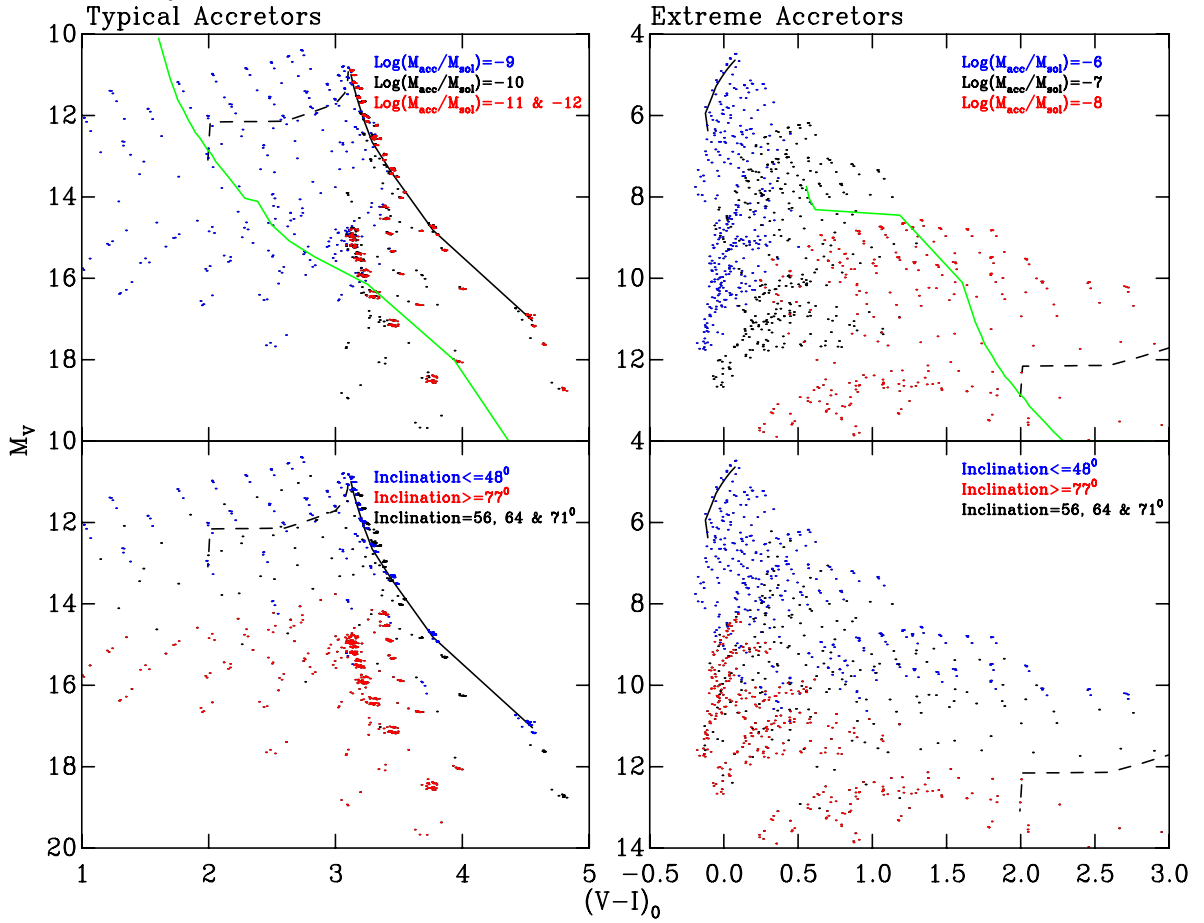


Figure 8. Figure showing CMDs in M_V , $(V-I)_0$ for typical accretors ($\log \dot{M} \leq -9$) in the left panels, and extreme accretors ($\log \dot{M} > -9$) in the right panels. The black dashed and solid lines correspond to naked BD isochrones (from our grid) with $\log \dot{M} = -9$ and -12 for the left panels (typical accretors) and -9 and -6 in the right panels (extreme accretors). The rotation rates and areal coverages are set at 5 days and 10% respectively (changing these has little effect). The top panels also include as a solid green line the 1 Myr pre-MS isochrone of Siess et al. (2000) adjusted to a distance modulus of 7 and an extinction of $A_V = 2$, simulating a reddened background population. The top panels then separate the systems by accretion rate with $\log \dot{M} = -9$, -10 and -11 & -12 in the top left panel, and $\log \dot{M} = -6$, -7 and -8 in the top right panel, shown blue, black and red dots respectively for both cases. The lower panels then split the systems into groups by inclination, with $\theta \leq 48^\circ$, $\theta \geq 77^\circ$ and $\theta = 56$, 64 & 71° , plotted as blue, red and black dots respectively.

4.3.2 Disc Fractions

Disc fractions have been derived using infrared excesses previously in JHK (e.g Lada & Lada 1995; Carpenter et al. 1997), however recent works pre-dominantly use *Spitzer* IRAC magnitudes (e.g Luhman et al. 2005, 2008; Gutermuth et al. 2008; Monin et al. 2010). Furthermore, MIPS magnitudes are used to identify so-called debris discs, where IR excesses are not apparent at shorter wavelengths (e.g Currie et al. 2008; Bryden et al. 2009). Finally, disc fractions have also been derived using the α criteria, where $\alpha = \frac{d\log \lambda F_\lambda}{d\log F_\lambda}$ between two limiting wavelengths, originally used to distinguish amongst Class I, II or II sources, but now used to detect disc presence (Lada et al. 2006; Kennedy & Kenyon 2009). An $\alpha > -2$ is used as a selection criterion for disc presence for TTS stars. We have constructed the α values for our model grid by adopting the limiting wavelengths of Kennedy & Kenyon (2009), namely 3.6 to $8.0\mu\text{m}$.

Figure 10 shows the photometry for all models in our grid in a $(J-K)_0$, $(J-H)_0$ CoCoDs. In all panels all of the naked systems are shown as black crosses. The left panels

show those systems with typical accretion rates and the right panels the extreme accretors. The top panels of Figure 10 then separate the systems by accretion rate with $\log \dot{M} = -9$, -10 and -11 & -12 , and -6 , -7 and -8 , shown as blue, black and red dots respectively for the typical (top left panel) and extreme (top right panel) accretors. The bottom panels then show the defined groups of inclination angles, with $\theta \leq 48^\circ$ as blue dots, $\theta > 56$ & 64° as black dots and $\theta \geq 71^\circ$ as red dots.

Figure 10 shows that there is, for both typical and extreme accretors, an overlap between the naked and BDD systems. This suggests that an empirically placed cut in a CoCoD of this type (in the absence of complications from variable reddening) could mis-identify some candidates. However, as disc fractions defined by placing a colour-colour cut are viewed as lower limits this effect may be small. Our grid show no correlation in a CoCoD of this type with rotation rate. In the case of the extreme accretors (right panels) there is a strong correlation of accretion rate and scatter from the naked stars. Additionally, the extreme accretors lie significantly removed from the naked stars locus. There is a

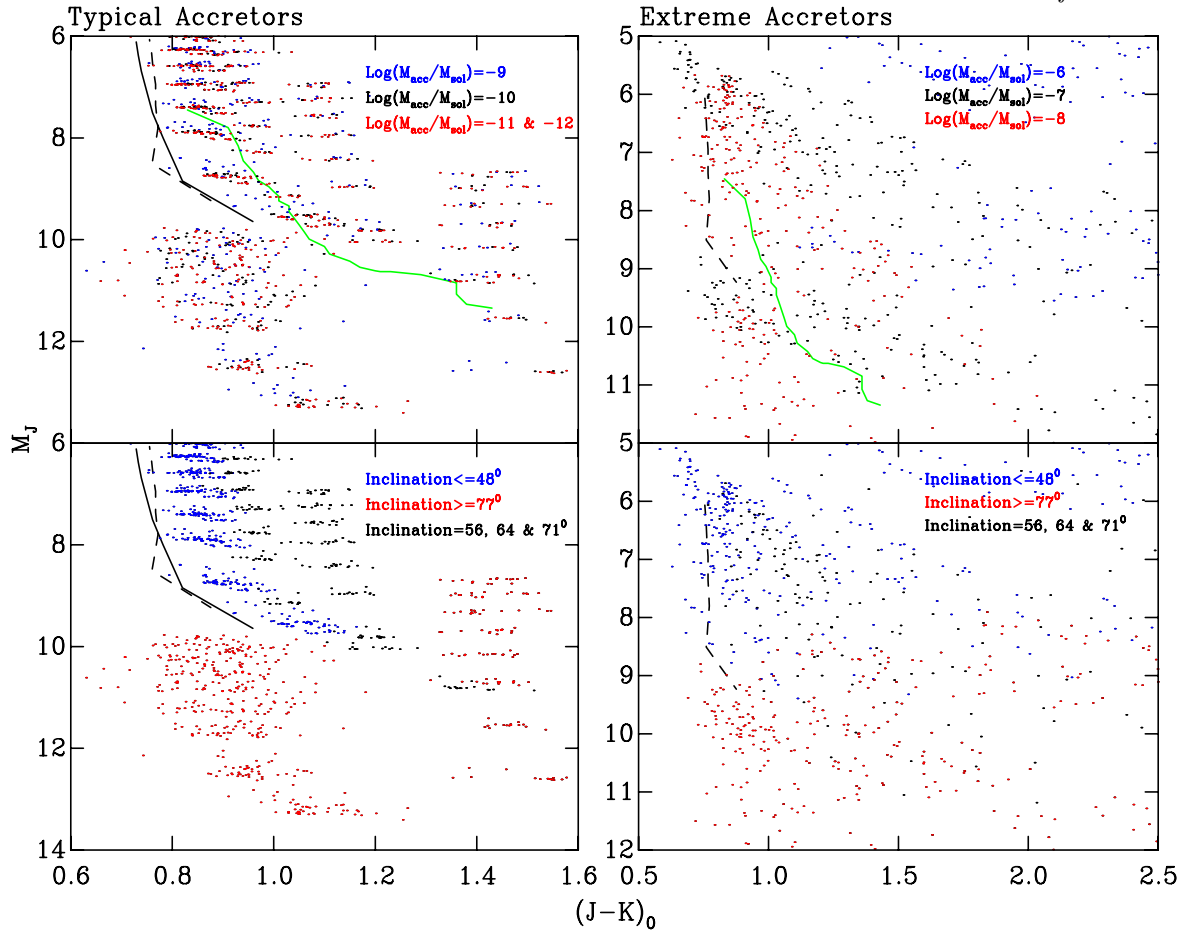


Figure 9. Figure showing the same data in the same format and with the same symbol meanings as Figure 8, but for M_J and $(J - K)_0$ CMDs. However, for this Figure the $\log M = -6$ isochrone is not shown (lies significantly blueward of locus of data), and the pre-MS isochrone of Siess et al. (2000), has been smoothed.

possibility that some of these objects may be lost due to saturation and limiting magnitude effects. Again, as with mass and age derivation, the present figures are representative of similar figures using alternative, similar magnitudes.

CoCoDs constructed using longer the longer wavelength bands of the IRAC and MIPS cameras are most commonly used for disc fraction calculation. Selection based on these types of data are well accepted as indicators of disc presence. Figures 11 and 12 show example CoCoDs for IRAC and MIPS magnitudes respectively.

Figures 11 and 12 show the same data in the same format with the same symbol meanings as Figure 10, except the colour indices. Figure 11 shows $([3.6] - [4.5])_0$, $([4.5] - [5.8])_0$ CoCoDs and Figure 12 shows a $(24 - 70)_0$, $(70 - 160)_0$ CoCoDs. Figure 12 also shows, as insets within the top panels, a larger scale figure to include the naked systems.

Figure 11 shows that, as expected, the IRAC CoCoDs clearly separate the naked and BDD systems. Once again, as found in Figure 10, for the extreme accretors the separation of the BDD systems from the naked stars is a weak function of accretion rate. There is also a weak correlation with inclination, with the face-on and expected systems closer to the naked stars. Figure 11 is representative of CoCoDs constructed using other IRAC photometric channels. As we include longer wavelength bands in the IRAC CoCoDs the

separation between the disc and naked loci increases. As the wavelength gets longer the flux originates from regions of the disc at lower temperature and therefore greater radial distance from the star. As photometric emission is minimal past around $3\mu\text{m}$, systems with discs will have significantly different SEDs from naked systems.

Figure 12 shows that as we increase the wavelength even further, into the range of the MIPS photometric bands, the separation between naked and BDD systems increases still further. The inset panels show that the separation between the naked and BDD systems is larger than in Figure 11. Additionally, there are clear correlations of MIPS positions with accretion rate and inclination. For the extreme accretors the systems are clearly delineated by accretion rate and inclination. This is as the emission is coming from greater radial positions within the disc where the structure of the disc is a finer function of the input variables.

Therefore, for models within our grid, disc fractions can be easily derived using IRAC and MIPS data. Whereas, JHK data used to derive a disc fraction will lead to a probable underestimate of the disc fraction. There also appears a correlation, especially for the extreme accretors, with position in the CoCoDs and accretion rate (and perhaps inclination).

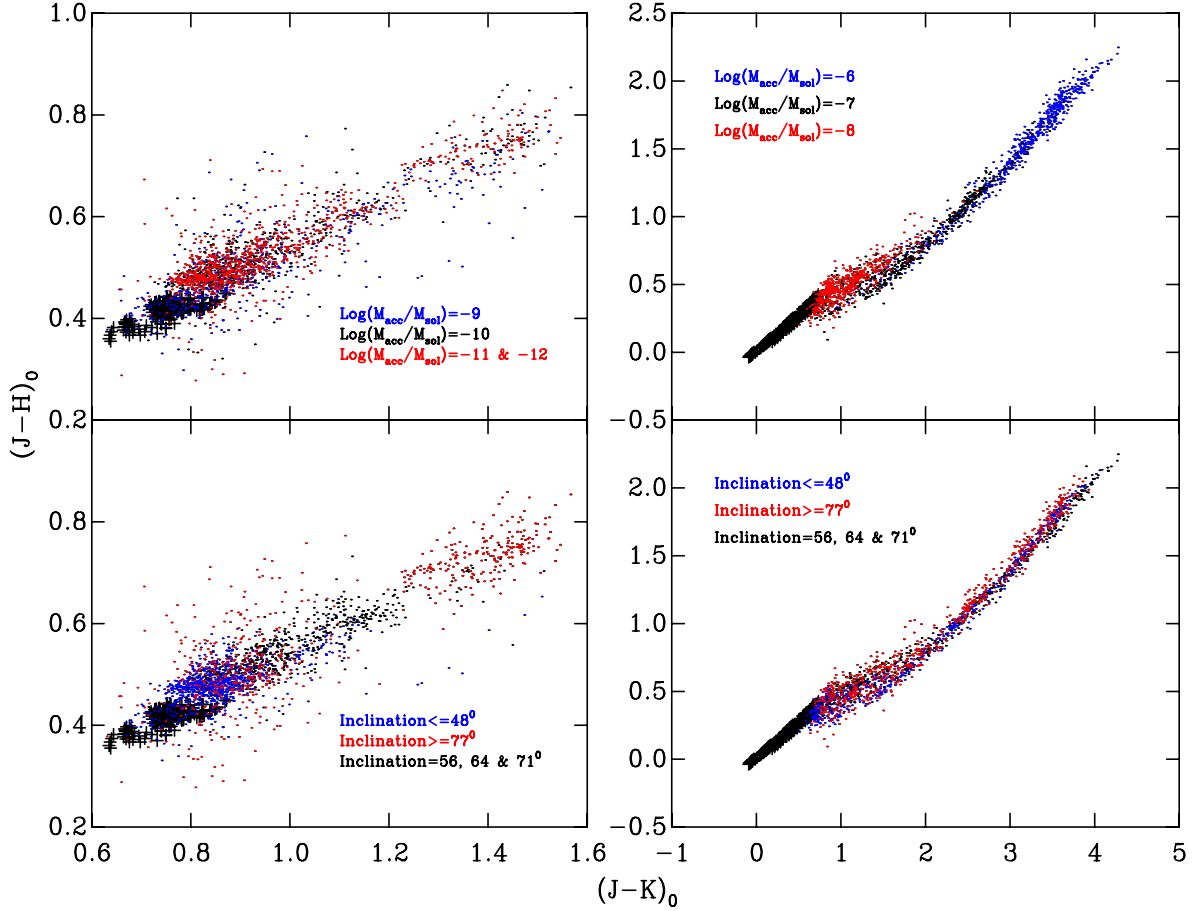


Figure 10. Figure showing $(J - K)_0$, $(J - H)_0$ CoCoDs for typical (left panel) and extreme accreting (right panels) systems. The top panels then separate the accretion rates with $\log \dot{M} = -9$, -10 and -11 & -12 , and $\log \dot{M} = -6$, -7 & -8 shown as blue, black and red dots respectively for the typical (top left panel) and extreme (top right panel) accretors. The bottom panels then show the systems with the inclinations $\theta \leq 48^\circ$ as blue dots, $\theta > 56$ & 64° as black dots and $\theta \geq 71^\circ$ as red dots.

4.3.3 Observational cuts

Recent derivations of disc fraction usually use colour-colour selection in the IRAC photometric bands. As we have shown within our model grid the separation between the BDD and naked systems is clear. Therefore, we can examine the success of some recent observationally placed when applied to our model grid. Additionally, disc fractions have been derived using the α value (Lada et al. 2006), essentially a slope of the SED between two wavelengths (at wavelengths longer than the stellar flux peak). As these α values are usually derived at wavelengths across the IRAC bands one would expect the resulting disc fractions to be reliable.

Figure 13 presents all the data for our model grid separated by age, with 1 and 10 Myr BDD systems shown as blue and red dots respectively. The naked systems are shown as black crosses. The CoCoDs featured are from several recent publications where disc fractions have been derived. The selection criteria from these studies are marked as dashed vertical and horizontal lines. The left panels show the typical accretors and the right panels the extreme accretors.

The observational cuts applied, shown as dashed lines, are from Luhman et al. (2005) a study of IC348, Luhman et al. (2008) a study of σ Orionis and Monin et al. (2010) (using the criteria of Gutermuth et al. 2008) a study of

the Taurus region. In these cases the effects of extinction are either negligible in the plotted colours, with values of $E([3.6] - [4.5]) < 0.04$ and $E([4.5] - [5.8]) < 0.02$ for IC348 and $A_V \leq 4$ mag (which will be negligible in the IRAC CoCoD, Allen et al. 2004), or the cuts have been placed in intrinsic colour space as for σ Orionis. The cuts from Luhman et al. (2005), Luhman et al. (2008) and Monin et al. (2010) appear as the top, top-middle and bottom-middle panels. The lower panel shows a recent BDD candidate selection using the α value from (Kennedy & Kenyon 2009).

Figure 13 shows that the recent observational cuts used to identify disc candidates would be, in the main, reliable for our model grid. Simulated photometry would be correctly identified using these cuts. It is important to note that our conclusions so far have been drawn from differential photometric arguments, in this case we are using intrinsic colours and these values are extremely sensitive to changes in zero point and photometric calibration. The top panel of Figure 13 shows that other than a few typically accreting systems the observational cut of Luhman et al. (2005) would select all of the BDD systems in our grid. The second panel down shows that the cut of Luhman et al. (2008) would miss some typical and a very small number of extreme accreting BDD systems (almost all are edge-on systems). The third panel down shows only very few BDD systems will be missed by

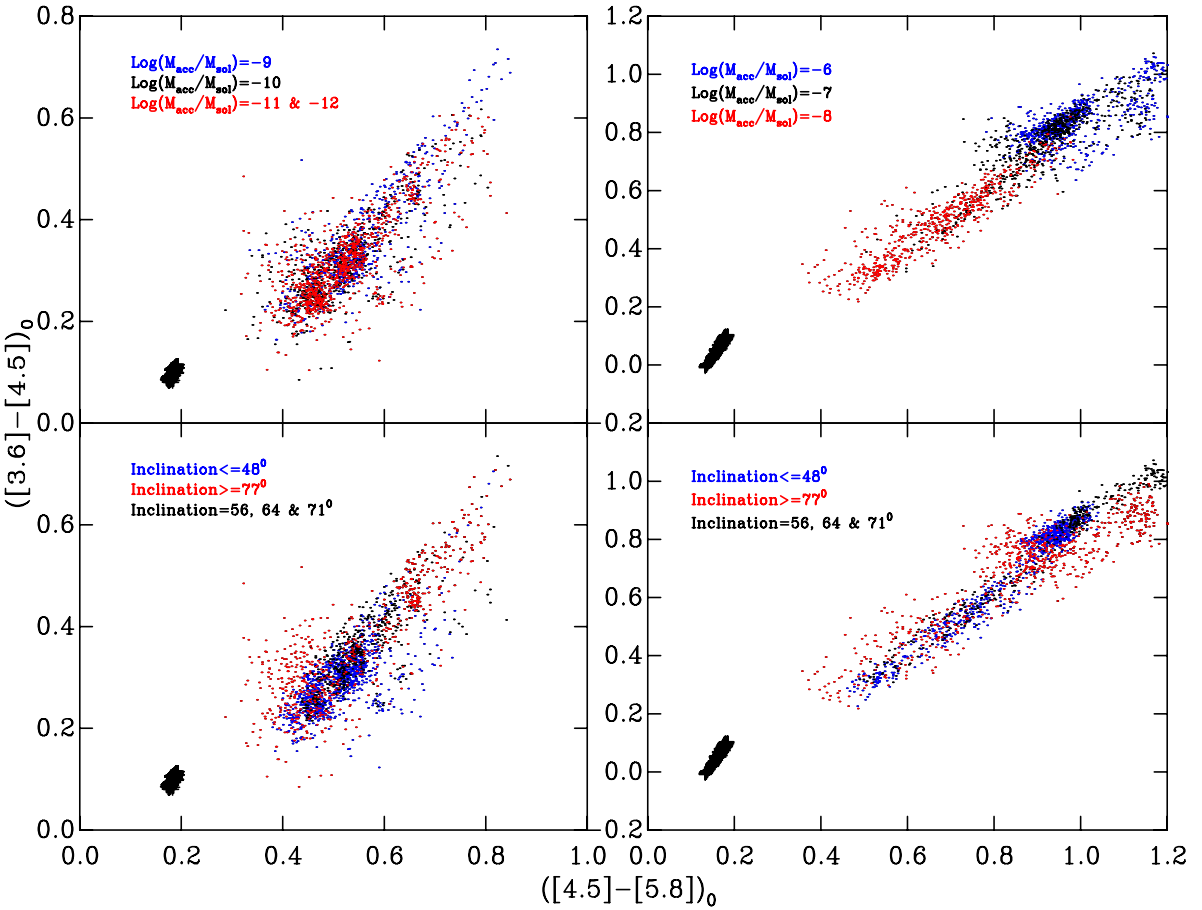


Figure 11. Figure showing $([3.6] - [4.5])_0$, $([4.5] - [5.8])_0$ CoCoDs of both typical (left panels) and extreme (right panels) accretors. The panels separate the different accretion rates and inclinations as in Figure 10.

the selection of Gutermuth et al. (2008) which was applied to Taurus by Monin et al. (2010). Finally, the selection for CTTS candidates of $\alpha > -2$ (Kennedy & Kenyon 2009) appears reasonably applicable to our BDD systems. As can be seen in the bottom panel of Figure 13 almost all the typical, and all of the extreme accreting BDD systems would be successfully identified using this criterion. Again the missed typically accreting systems are edge-on systems. Given that extreme reddening may move naked stars into the BDD region selected, in general, disc fractions are usually quoted as lower limits. Therefore, a small number of miss-identified BDD system is a negligible effect. This allows us to conclude, that ubiquitously used BDD selections within IRAC CoCoDs are reliable when applied to our model grid. Additionally, the α value would be a reliable disc indicator for our model grid.

Using our model grid we can define the optimal cuts for selecting BDD systems. These are shown in Table 2, where the defined cuts are chosen to minimise contamination from naked stars.

5 CONCLUSIONS

We have constructed a model grid of SEDs, and subsequently photometric magnitudes and colours, for actively accreting BDs with or without an associated accretion disc.

Colour index	Disc selection	Number missed (# & %)
$\alpha(3.6 - 8.0)_0$	> -2.20	26/4480=0.6%
$([3.5] - [4.5])_0$	$> +0.21$	201/4480=4.5%
$([3.5] - [5.8])_0$	$> +0.50$	12/4480=0.3%
$([4.5] - [5.8])_0$	$> +0.32$	9/4480=0.2%
$([4.5] - [8.0])_0$	$> +0.45$	7/4480=0.2%
$([5.8] - [8.0])_0$	$> +0.13$	13/4480=0.3%
$([8.0] - 24)_0$	> -16.2	0/4480=0.0%
$(24 - 70)_0$	$> +9.90$	2/4480=0.04%
$(70 - 160)_0$	> -6.20	0/4480=0.0%

Table 2. List of all the cuts which when applied to our simulated dataset provide the best disc candidate selection with minimised contamination.

We have modeled the photospheric flux from these BDs by adopting (and interpolating) the interior ‘DUSTY00’ models of Chabrier et al. (2000) combined with the ‘AMES-Dusty’, atmospheric models of Chabrier et al. (2000). We have then assumed that accretion occurs from an inner edge of a magnetically truncated accretion disc (truncated at the co-rotation radius). The accretion flux is calculated using a simple blackbody emission, given the derivation of a characteristic spot effective temperature. SEDs were then produced for both naked BDs and BDD systems. For the BDD systems we have modeled the disc using the TORUS radiative

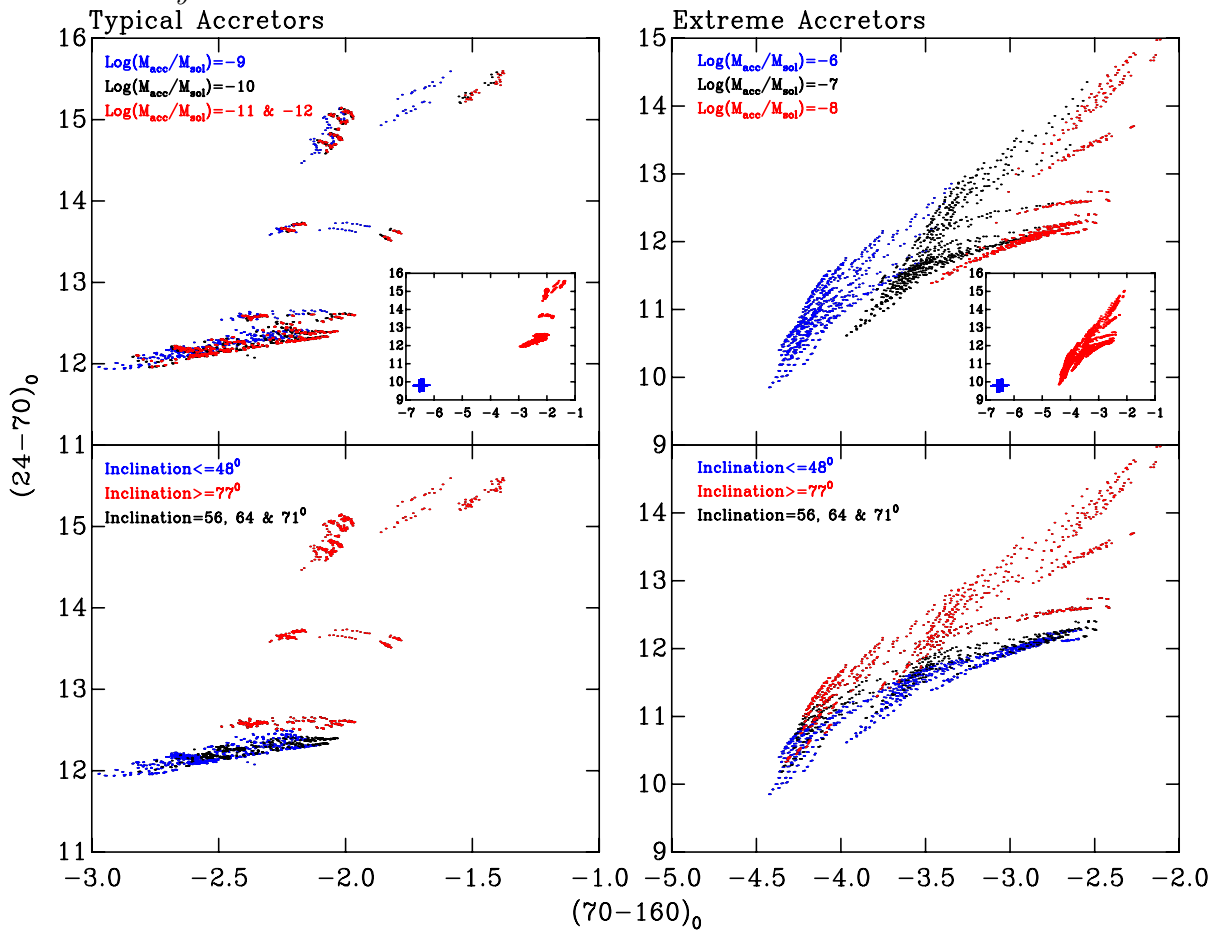


Figure 12. Figure showing $(24 - 70)_0$, $(70 - 160)_0$ CoCoDs in the same format as Figure 10. The smaller inset panels in the top panels show the separation between the naked (blue crosses) and BDD systems (red dots).

transfer code using the Lucy (1999) radiative equilibrium algorithm and incorporating dust sublimation and including a treatment of vertical hydrostatic equilibrium (see Section 2 for a discussion of the code). In order to produce a grid of simulated systems we have varied several input parameters namely: stellar mass, stellar age, stellar rotation rate, accretion rate, the areal coverage of the accretion stream and the system inclination (the disc mass was fixed). The ranges of these variables were selected to represent and bound typical BD systems, justification is provided using evidence from observational studies in Section 3 and a final list of the values of these variables can be found in Table 1.

Accepting our assumptions, parameter ranges and radiative transfer code our resulting simulated dataset has allowed us to qualitatively explore the effects of *active* (current not past) accretion on disc structure. Furthermore through the simulation of observations we have explored the effects of accretion, and disc presence, on both the SEDs, and photometric colours and magnitudes of these systems.

As discussed in Section 4.1 vertical hydrostatic equilibrium, when applied to BDs, leads to increased flaring, when compared to CTTS. This has previously been explored by Walker et al. (2004). However, in our study we have included a simple treatment of accretion. This leads to increased flaring as more flux reaches the outer disc, and subsequently lower inclinations angles at which the central star is ob-

scured for BDD systems with higher accretion rates. Furthermore, the addition of dust sublimation has shown that for BDD systems the inner disc location, temperature and vertical size and shape also varies with accretion rate. The inner edge position is correlated with temperature for the lower accreting models as suggested by Meyer et al. (1997). For the systems with higher accretion rates the inner edge temperature is weakly correlated with temperature, mainly due to the radial fall in density and therefore dust sublimation temperature. The inner disc edge, initially prescribed as a vertical wall, then becomes concave and finally convex as dust sublimation is increased (with increasing flux from higher rates of accretion).

Subsequently the SEDs of BDD systems with typical accretion rates and associated discs change significantly from the assumed underlying photospheric model flux, and therefore become difficult to classify. In Section 4.2 we have shown that the BD photosphere becomes veiled by the accretion flux for rates of $\log \dot{M} > -9$. The outer disc flaring observed in the BDD systems was shown to cause occultation and a subsequent, sharp, fall in flux at an inclination which decreases for more systems with higher accretion rates. We have also shown that for extreme accretion rates the inner wall increases in size and becomes convex in shape.

Subsequent derivation of photometric magnitudes has allowed us to demonstrate that, as expected, increased ac-

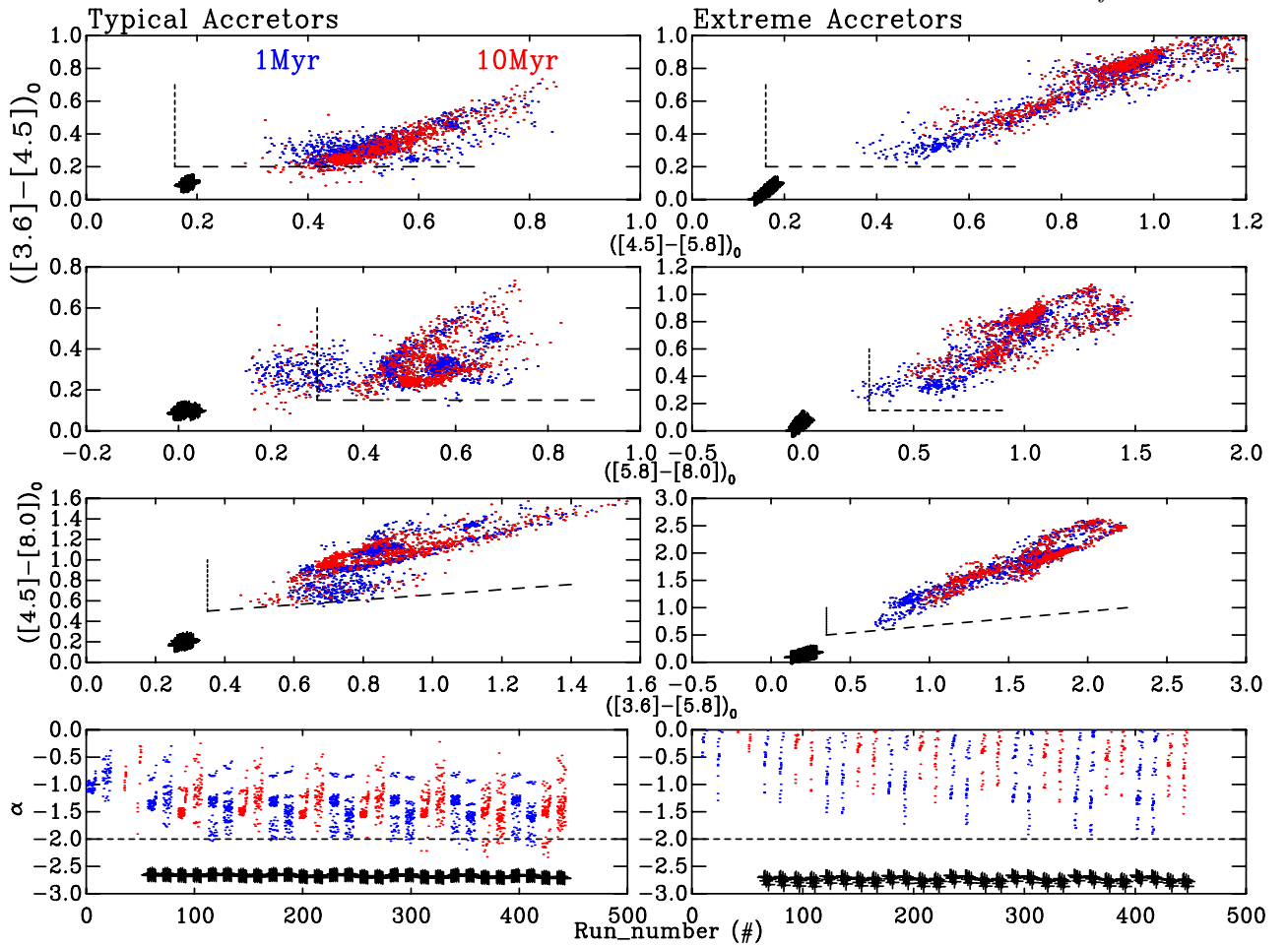


Figure 13. Figure showing both from top to bottom, the disc candidate selection of Luhman et al. (2005), Luhman et al. (2008), Monin et al. (2010) (using the criteria of Gutermuth et al. 2008) and Kennedy & Kenyon (2009). The photometry or α values for all models are shown, with naked stars as black crosses, 1 Myr BDD systems as blue dots and 10 Myr BDD systems as red dots. The dashed horizontal and vertical lines are disc selections from the studies in question. The left panels are the typical accretors and the right panels the extreme accretors. The top three panels are IRAC CoCoDs and the bottom panel plots the α value against run number (an arbitrary number).

cretion without disc presence, moves our naked systems to bluer and brighter magnitudes. Once a disc is added the increase in accretion flux interacts with the disc and does not necessarily lead to a simple motion toward brighter magnitudes and bluer colours. The increased flaring and obscuration present in BDD systems, over CTTS, leads to rapid falls in magnitude with inclination as an accretion (or flaring) dependent inclination. Furthermore, the disc inner edge leads to a shift redwards with increasing accretion rate as more flux is intercepted by the inner edge and the inner edge becomes convex and ‘puffed up’.

In practice most parameters for BDD systems are derived for populations. We have shown, in Section 4.3 that derivation of an *isochronal* (or photometric) age from our simulated photometry of a coeval BD sample, with typical accretion rates and associated circumstellar discs, would be inaccurate and exceedingly difficult. Indeed, the resulting photometric colours and magnitudes could be indicative of a more distant, and with higher extinction levels, CTTS population. For more extreme accretion rates the scatter (in CMD space) is significantly far from the naked BD locus

and as such these stars have little chance of being selected as BDs. As discussed in Section 4 this does not include any effects due to past accretion on the evolution of the central star, which acts to accelerate the gravitational contraction and make the star appear older (Tout et al. 1999; Siess et al. 1999), further scattering the apparent age of a coeval population. Concordantly, *isochronal* derivations of mass and therefore IMFs, for our simulated photometry, of a coeval population of accreting BDs with associated discs, would be inaccurate and problematic. Again this caused by the changes in the SEDs as a result of the accretion flux and increased occultation by the larger degree of flaring seen in BD discs (for the latter, as found by Walker et al. 2004)

We have also qualitatively explored the effects of accretion and disc presence in our simulated dataset on disc fraction estimates. As is currently well known, longer wavelength bandpasses are much more reliable and suitable for disc identification. As shown in Section 4 the naked and BDD disc loci were much more clearly separated in the CoCoD constructed using *Spitzer* IRAC magnitudes than the shorter wavelength CIT JHK passbands. In addition, we that the

slope of the SED from 3.6 to $8.0\mu\text{m}$, or α value, is an effective disc indicator. We have also tentatively shown that current observational cuts, when applied to our simulated photometry (with its associated photometric system), results in the reliable detection of disc candidates for IRAC and MIPS colours and α values, and therefore a robust lower limit disc fraction. Cuts derived from our model grid which could be used as a guide for observational disc candidate selection are presented in Table 2.

A further area this study impacts on (perhaps most significantly) is the recent evidence for a stellar mass to accretion rate correlation, of the approximate form: $\dot{M}_{\text{acc}} \propto M_*^2$ (Mueller et al. 2003; Natta et al. 2004, 2006). This relationship has been extended into the BD mass regime in Natta et al. (2006). However, arguments based on selection and detection thresholds have already cast this relation into doubt (Clarke & Pringle 2006). As we have shown in Section 4 a relationship of this kind is self-reinforcing as lower mass objects with higher accretion rates have little chance of being correctly identified as such due to both the accretion flux and flared associated disc. Essentially, at present it is unclear how many BDs are not included in this relationship due to misidentification. As explained in Walker et al. (2004), BD systems with a disc, without including accretion effects, can have the characteristics of higher mass CTTS stars, due to increased disc flaring from a reduced surface gravity in the disc. The effects of accretion at typical or larger rates further exacerbate the situation both spectroscopically, as the photospheric flux essentially becomes swamped or completely veiled, and photometrically as the resulting colours and magnitudes are significantly shifted. Therefore, for our simulated dataset a relationship of this sort may well be derived, if typical methods are used to identify BD objects with discs and derive masses, ages and accretion rates, even though it is not present.

Finally, although inner edge locations are correlated with their temperature we do not find a resulting correlation with IR excess. As our initial inner edge locations are placed at the co-rotation radius one might expect a correlation between rotation rate and IR excess. This in turn might suggest that studies of disc presence correlation with slower rotation rates, exploring disc-locking, may have intrinsic biases. However, for our systems with dust sublimation, vertical flaring, accretion and view over a range of inclinations any correlation is not apparent.

We intend to extend the range of BBD models, employing both an increased parameter space and also a set of models adopting analytical prescriptions of the disc structure (as opposed to hydrostatic equilibrium). We are also extending our emission line modelling efforts (Kurosawa et al. 2006) to lower central star masses in order to identify both the location of the line emission in the light of the work by Gatti et al. (2006) and to examine the efficacy of line fluxes as an accretion rate probe. We are also extending our grid of CTTS magnetospheric accretion models to lower accretion rates in order to identify the limit at which low accretion rate CTTS are no longer identified as accreting from H α line flux and morphology.

ACKNOWLEDGMENTS

The simulations in this work were performed using the University of Exeter supercomputer, an SGI Altix ICE 8200. NJM and TJH were supported by STFC grant ST/F003277/1. We would also like to thank Dave Acreman for help with the practicality of running the model grid.

REFERENCES

- Allen L. E., Calvet N., D'Alessio P., Merin B., Hartmann L., Megeath S. T., Gutermuth R. A., Muzeirole J., Pipher J. L., Myers P. C., Fazio G. G., 2004, *ApJS*, 154, 363
- Allers K. N., Kessler-Silacci J. E., Cieza L. A., Jaffe D. T., 2006, *ApJ*, 644, 364
- Anders E., Grevesse N., 1989, *Geochim. Cosmochim. Acta*, 53, 197
- Asplund M., Grevesse N., Sauval A. J., 2006, *Communications in Asteroseismology*, 147, 76
- Barrado y Navascués D., Martín E. L., 2003, *AJ*, 126, 2997
- Bertout C., Harder S., Malbet F., Mennessier C., Regev O., 1996, *AJ*, 112, 2159
- Bessell M. S., 2000, *PASP*, 112, 961
- Bessell M. S., 2005, *ARA&A*, 43, 293
- Bessell M. S., Brett J. M., 1988, *PASP*, 100, 1134
- Bessell M. S., Castelli F., Plez B., 1998, *A&A*, 333, 231
- Bouvier J., Alencar S. H. P., Harries T. J., Johns-Krull C. M., Romanova M. M., 2007, in Reipurth B., Jewitt D., Keil K., eds, *Protostars and Planets V Magnetospheric Accretion in Classical T Tauri Stars*. pp 479–494
- Bouvier J., Covino E., Kovo O., Martin E. L., Matthews J. M., Terranegra L., Beck S. C., 1995, *A&A*, 299, 89
- Bouy H., Huélamo N., Pinte C., co authors., 2008, *A&A*, 486, 877
- Bryden G., Beichman C. A., Carpenter J. M., Rieke G. H., Stapelfeldt K. R., Werner M. W., Tanner A. M., Lawler S. M., Wyatt M. C., Trilling D. E., Su K. Y. L., Blaylock M., Stansberry J. A., 2009, *ApJ*, 705, 1226
- Camenzind M., 1990, in Klare G., ed., *Reviews in Modern Astronomy Vol. 3 of Reviews in Modern Astronomy, Magnetized Disk-Winds and the Origin of Bipolar Outflows..* pp 234–265
- Carpenter J. M., Meyer M. R., Dougados C., Strom S. E., Hillenbrand L. A., 1997, *AJ*, 114, 198
- Chabrier G., Baraffe I., Allard F., Hauschildt P., 2000, *ApJ*, 542, 464
- Clarke C. J., Pringle J. E., 2006, *MNRAS*, 370, L10
- Cohen M., Walker R. G., Barlow M. J., Deacon J. R., Witteborn F. C., Carbon D., Augason G., 1993, in Kwok S., ed., *Astronomical Infrared Spectroscopy: Future Observational Directions Vol. 41 of Astronomical Society of the Pacific Conference Series, Absolute Spectrally Continuous Stellar Irradiance Calibration in the Infrared.* pp 55–
- Cohen M., Wheaton W. A., Megeath S. T., 2003, *AJ*, 126, 1090
- Currie T., Kenyon S. J., Balog Z., Rieke G., Bragg A., Bromley B., 2008, *ApJ*, 672, 558
- Dahm S. E., Carpenter J. M., 2009, ArXiv e-prints
- Dullemond C. P., Dominik C., Natta A., 2001, *ApJ*, 560, 957
- Elias J. H., Frogel J. A., Matthews K., Neugebauer G., 1982, *AJ*, 87, 1029

- Ercolano B., Clarke C. J., Robitaille T. P., 2009, ArXiv e-prints
- Fukugita M., Ichikawa T., Gunn J. E., Doi M., Shimasaku K., Schneider D. P., 1996, AJ, 111, 1748
- Gatti T., Testi L., Natta A., Randich S., Muzeirole J., 2006, A&A, 460, 547
- Gullbring E., Hartmann L., Briceno C., Calvet N., Muzeirole J., 1998, in Donahue R. A., Bookbinder J. A., eds, Cool Stars, Stellar Systems, and the Sun Vol. 154 of Astronomical Society of the Pacific Conference Series, Color Anomalies of Weak Lined T Tauri stars. pp 1709–+
- Gutermuth R. A., Myers P. C., Megeath S. T., Allen L. E., Pipher J. L., Muzeirole J., Porras A., Winston E., Fazio G., 2008, ApJ, 674, 336
- Haisch Jr. K. E., Lada E. A., Lada C. J., 2001, ApJL, 553, L153
- Harries T. J., 2000, MNRAS, 315, 722
- Harries T. J., Monnier J. D., Symington N. H., Kurosawa R., 2004, MNRAS, 350, 565
- Hartmann L., 1998, Accretion Processes in Star Formation. Accretion processes in star formation / Lee Hartmann. Cambridge, UK ; New York : Cambridge University Press, 1998. (Cambridge astrophysics series ; 32) ISBN 0521435072.
- Hawarden T. G., Leggett S. K., Letawsky M. B., Ballantyne D. R., Casali M. M., 2001, MNRAS, 325, 563
- Herbst W., Eislöffel J., Mundt R., Scholz A., 2007, in Reipurth B., Jewitt D., Keil K., eds, Protostars and Planets V The Rotation of Young Low-Mass Stars and Brown Dwarfs. pp 297–311
- Herczeg G. J., Cruz K. L., Hillenbrand L. A., 2009, ArXiv e-prints
- Holland W. S., Robson E. I., Gear W. K., Cunningham C. R., Lightfoot J. F., Jenness T., Ivison R. J., Stevens J. A., Ade P. A. R., Griffin M. J., Duncan W. D., Murphy J. A., Naylor D. A., 1999, MNRAS, 303, 659
- Isella A., Natta A., 2005, A&A, 438, 899
- Jayawardhana R., Ardila D. R., Stelzer B., Haisch Jr. K. E., 2003, AJ, 126, 1515
- Joergens V., Fernández M., Carpenter J. M., Neuhauser R., 2003, ApJ, 594, 971
- Johnson H. L., 1966, ARA&A, 4, 193
- Kama M., Min M., Dominik C., 2009, A&A, 506, 1199
- Kennedy G. M., Kenyon S. J., 2009, ArXiv e-prints
- Kenyon S. J., Hartmann L., 1995, ApJS, 101, 117
- Koenigl A., 1991, ApJL, 370, L39
- Kurosawa R., Harries T. J., Bate M. R., Symington N. H., 2004, MNRAS, 351, 1134
- Kurosawa R., Harries T. J., Symington N. H., 2006, MNRAS, 370, 580
- Lada C. J., Muench A. A., Luhman K. L., Allen L., Hartmann L., Megeath S. T., Myers P., Fazio G., Wood K., Muzeirole J., Rieke G., Siegler N., Young E., 2006, AJ, 131, 1574
- Lada E. A., Lada C. J., 1995, AJ, 109, 1682
- Leggett S. K., 1992, ApJS, 82, 351
- Lucy L. B., 1999, A&A, 344, 282
- Luhman K. L., D'Alessio P., Calvet N., Allen L. E., Hartmann L., Megeath S. T., Myers P. C., Fazio G. G., 2005, ApJL, 620, L51
- Luhman K. L., Hernández J., Downes J. J., Hartmann L., Briceño C., 2008, ApJ, 688, 362
- Luhman K. L., Lada C. J., Hartmann L., Muench A. A., Megeath S. T., Allen L. E., Myers P. C., Muzeirole J., Young E., Fazio G. G., 2005, ApJL, 631, L69
- Martín E. L., Brandner W., Bouvier J., Luhman K. L., Stauffer J., Basri G., Zapatero Osorio M. R., Barrado y Navascués D., 2000, ApJ, 543, 299
- Mayne N. J., Naylor T., 2008, MNRAS, 386, 261
- Mayne N. J., Naylor T., Littlefair S. P., Saunders E. S., Jeffries R. D., 2007, MNRAS, 375, 1220
- Meyer M. R., Calvet N., Hillenbrand L. A., 1997, AJ, 114, 288
- Mohanty S., Jayawardhana R., Natta A., Fujiyoshi T., Tamura M., Barrado y Navascués D., 2004, ApJL, 609, L33
- Mohanty S., Shu F. H., 2008, ApJ, 687, 1323
- Monin J., Guieu S., Pinte C., Rebull L., Goldsmith P., Fukagawa M., Ménard F., Padgett D., Stappeldorf K., McCabe C., Carey S., Noriega-Crespo A., Brooke T., Huard T., Terebey S., Hillenbrand L., Guedel M., 2010, ArXiv e-prints
- Morrow A. L., Luhman K. L., Espaillat C., D'Alessio P., Adame L., Calvet N., Forrest W. J., Sargent B., Hartmann L., Watson D. M., Bohac C. J., 2008, ApJL, 676, L143
- Muzeirole J., Hillenbrand L., Calvet N., Briceño C., Hartmann L., 2003, ApJ, 592, 266
- Muzeirole J., Luhman K. L., Briceño C., Hartmann L., Calvet N., 2005, ApJ, 625, 906
- Najita J. R., Strom S. E., Muzeirole J., 2007, MNRAS, 378, 369
- Natta A., Testi L., Comerón F., Oliva E., D'Antona F., Baffa C., Comoretto G., Gennari S., 2002, A&A, 393, 597
- Natta A., Testi L., Muzeirole J., Randich S., Comerón F., Persi P., 2004, A&A, 424, 603
- Natta A., Testi L., Randich S., 2006, A&A, 452, 245
- Neugebauer G., Habing H. J., van Duinen R., co authors ., 1984, ApJL, 278, L1
- Noels A., Grevesse N., 1993, in Weiss W. W., Baglin A., eds, IAU Colloq. 137: Inside the Stars Vol. 40 of Astronomical Society of the Pacific Conference Series, Small and intermediate mass stellar evolution - Main sequence and close to it. pp 410–425
- Pascucci I., Apai D., Luhman K., Henning T., Bouwman J., Meyer M., Lahuis F., Natta A., 2008, ArXiv e-prints
- Pinte C., Harries T. J., Min M., Watson A. M., Dullemond C. P., Woitke P., Ménard F., Durán-Rojas M. C., 2009, A&A, 498, 967
- Pollack J. B., Hollenbach D., Beckwith S., Simonelli D. P., Roush T., Fong W., 1994, ApJ, 421, 615
- Rice W. K. M., Wood K., Armitage P. J., Whitney B. A., Bjorkman J. E., 2003, MNRAS, 342, 79
- Robitaille T. P., Whitney B. A., Indebetouw R., Wood K., Denzmore P., 2006, ApJS, 167, 256
- Scholz A., Eislöffel J., 2004, A&A, 419, 249
- Scholz A., Eislöffel J., 2005, A&A, 429, 1007
- Shakura N. I., Sunyaev R. A., 1973, A&A, 24, 337
- Shu F., Najita J., Ostriker E., Wilkin F., Ruden S., Lizano S., 1994, ApJ, 429, 781
- Siess L., Dufour E., Forestini M., 2000, A&A, 358, 593
- Siess L., Forestini M., Bertout C., 1999, A&A, 342, 480
- Simons D. A., Tokunaga A., 2002, PASP, 114, 169
- Skrutskie M. F., Cutri R. M., Stiening R., co authors ., 2006, AJ, 131, 1163

- Stephens D. C., Leggett S. K., 2004, PASP, 116, 9
Tannirkulam A., Harries T. J., Monnier J. D., 2007, ApJ, 661, 374
Tokunaga A. T., Simons D. A., Vacca W. D., 2002, PASP, 114, 180
Tout C. A., Livio M., Bonnell I. A., 1999, MNRAS, 310, 360
Walker C., 2006, PhD thesis, University of St. Andrews
Walker C., Wood K., Lada C. J., Robitaille T., Bjorkman J. E., Whitney B., 2004, MNRAS, 351, 607
White R. J., Basri G., 2003, ApJ, 582, 1109
Wood K., Wolff M. J., Bjorkman J. E., Whitney B., 2002, ApJ, 564, 887
Zapatero Osorio M. R., Béjar V. J. S., Pavlenko Y., Rebolo R., Allende Prieto C., Martín E. L., García López R. J., 2002, A&A, 384, 937

APPENDIX A: WEBSITE

As stated throughout this paper the data presented are available from a web page⁷.

A1 Available Data

The magnitudes and colours presented in this paper are available both as individual magnitudes and as isochrones or mass tracks. Photometric magnitudes have also been derived for several other systems and are available online. These are Johnson, Cousins *UBVRI(JHK)* (Johnson 1966; Bessell 2005), *Tycho V_t* and *B_t* (Bessell 2000), Bessell *UBVRIJHKL* (Bessell & Brett 1988; Bessell et al. 1998), SDSS *UGRIZ* (Fukugita et al. 1996), 2MASS *JHK_s* (Cohen et al. 2003; Skrutskie et al. 2006), MKO *JHK* (Simons & Tokunaga 2002; Tokunaga et al. 2002), UKIRT *ZYJHK* (Hawarden et al. 2001), IRAS 12, 25, 60 and 100 μm (Neugebauer et al. 1984) and SCUBA *450WB* and *850WB* (Holland et al. 1999). For further information on these magnitudes, such as the filter responses used and the adopted zeropoints please refer to the website.

Monochromatic fluxes

In addition to the magnitudes derived for each of these bands monochromatic fluxes have also been derived for all bands listed above. These have been derived following closely the methods of Robitaille et al. (2006), extended to further passbands. For details of the assumed SED shape, central wavelengths and bandpasses adopted please refer to the website. The derivations of these monochromatic fluxes will be detailed in a coming paper, which details a fitting tool associated with these data.

APPENDIX B: CONSISTENCY CHECKS

Firstly, a check was made on the photospheric input flux and the resulting stellar direct flux (tagged by TORUS) after the radiative transfer simulation. The resulting flux distributions should match most closely for face-on configurations, and then match in shape only, with the stellar direct flux

⁷ http://www.astro.ex.ac.uk/research/bd_disc

level dropping towards higher inclinations, as more photons are scattered and absorbed by the disc.

We also directly compared the magnitudes and colours of our naked BD systems with the lowest accretion rate ($-12 \log(\frac{\dot{M}}{M_{\odot}} \text{yr}^{-1})$) to those published in Chabrier et al. (2000), in the same photometric system (*CIT*). We found significant colour differences ($\delta(J-K) \leq 0.1$), between our derived values and those of Chabrier et al. (2000). As a further check we derived the magnitudes in the Bessell et al. (1998) system (by both adopting the published zero points, and by using a Vega reference spectrum), and applied conversions of Leggett (1992)⁸, to the *CIT* system. For each method we failed to match the magnitudes and colours published in Chabrier et al. (2000). As a final test we passed the downloaded, unaltered, atmospheric spectra directly through the filter response program, without interpolation, for the closest matches in $\log(g)$ and T_{eff} from the interior models published in Chabrier et al. (2000). These magnitudes and colours also failed to match. Therefore, we must conclude that the most likely cause of the mismatch is due to improvements in the model atmospheres available online⁹ (this is likely as the models available online, have a later time stamp, ≈ 2005 compared to 2000). For the final published magnitudes, for the naked systems, we have used a similar wavelength resolution as in our BDD systems, i.e. 200 logarithmically spaced points. This means that magnitudes derived from these spectra will differ slightly from those derived from the full spectra, but this effect is negligible, and increased resolution for only some of our model grid (i.e. naked stars) will hamper comparison between the models.

The final test of the derived colours and magnitudes was a comparison of the naked systems with the results for the almost face-on BDD systems. The results for the optical passbands should be similar and an appraisal of the component SED, i.e. showing the stellar direct flux.

We have adopted zeropoints derived using a Vega reference spectrum for the optical and near-IR passbands. As a test we have compared our derived zeropoints using the filter response of Bessell et al. (1998) and the Vega reference spectrum against those published in Bessell et al. (1998). For our photometric systems we integrate the summed number of photons counted by the simulated telescope systems, however to test the zeropoints and match the system of Bessell et al. (1998) we must integrate the summed energy. The zeropoints we derived (with the values of Bessell et al. 1998, in parenthesis) were: $U = 20.977(20.94)$, $B = 20.499(20.498)$, $V = 21.116(21.10)$, $R = 21.676(21.655)$, $I = 22.376(22.371)$, $J = 23.735(23.755)$, $H = 24.989(24.860)$, $K = 25.884(26.006)$ and $L = 27.809(27.875)$. Our derived zeropoints and those of Bessell et al. (1998) match to within 0.05 mags (and usually much closer) for all bands except the *H,K* and *L* bands. This is probably due to the previously noted IR excess (although detected at longer wavelengths) of the observed Vega spectrum. Bessell et al. (1998) use a combined model spectrum of Vega and Sirius as their reference spectrum. As a further test we also used the synthetic A0V stellar spectrum of Cohen et al. (1993) to derive zeropoints but were still unable

⁸ We have also included the wavelength shift mentioned in Stephens & Leggett (2004)

⁹ <http://perso.ens-lyon.fr/france.allard/>

to improve the match to the Bessell et al. (1998) photometric system for the *JHK* colours. However, for these colours we have adopted the *CIT* system, but were unable to find published zeropoints, and therefore used the Vega reference spectrum. Essentially this may mean there is a small offset in our *JHK* photometry, however as most of our results are based on differential photometry this will not affect our conclusions.

A further complication with our adopted photometric systems is the range of zeropoints available for the *Spitzer* IRAC photometry. For this study, as stated, we have adopted zeropoints calculated using the zero magnitude flux from the IRAC handbook¹⁰. The resulting zeropoints were: Channel 1[3.6]=19.541, channel 2[4.5]=19.089, channel 3[5.8]=17.395 and channel 4[8.0]=17.966. The corresponding zeropoints derived for the MIPS passbands were: channel 1[24]=-2.139, channel 2[70]=-0.2726 and channel 3[160]=-1.990.

In summary, several careful consistency checks were performed to confirm that the resulting SEDs and photometric magnitudes behaved as expected and matched any available published results. A failure to match the published zeropoints in the near-IR bands of the Bessell et al. (1998) using a Vega reference spectrum was probably due to an IR excess in our observed Vega spectrum. However as in general most of the conclusions or implications of this study are based on differential photometry, this should not affect them adversely. Furthermore, a failure to match the published magnitudes (and colours) for the atmospheric models in Chabrier et al. (2000), even using published zeropoints for the excellently defined system of Bessell et al. (1998), and subsequent conversions to the required *CIT* system (Leggett 1992), was prescribed to an update in the model atmospheres available online.

¹⁰ <http://ssc.spitzer.caltech.edu/documents/som/som8.0.irac.pdf>